Article

Assessing the Validity of Negative High Field Strength-Element Anomalies as a Proxy for Archaean Subduction: Evidence from the Ben Strome Complex, NW Scotland

George L. Guice [1],* , **Iain McDonald [1]** , **Hannah S. R. Hughes [2,3]** , **Denis M. Schlatter [4]** ,
Kathryn M. Goodenough [5] , **John M. MacDonald [6]** and **John W. Faithfull [7]**

[1] School of Earth and Ocean Sciences, Cardiff University, Cardiff CF10 3AT, UK; McDonaldI1@cardiff.ac.uk
[2] Camborne School of Mines, Tremough Campus, University of Exeter, Penryn TR10 9EZ, UK;
    H.Hughes@exeter.ac.uk
[3] School of Geosciences, University of the Witwatersrand, Wits 2050 Johannesburg, South Africa
[4] Helvetica Exploration Services GmbH, CH-8053 Zürich, Switzerland;
    denis.schlatter@helvetica-exploration.ch
[5] British Geological Survey, Lyell Centre, Edinburgh EH14 4AP, UK; kmgo@bgs.ac.uk
[6] School of Geographical and Earth Sciences, Gregory Building, University of Glasgow,
    Glasgow G12 8QQ, UK; John.MacDonald.3@glasgow.ac.uk
[7] Hunterian Museum, University of Glasgow, Glasgow G12 8QQ, UK; John.Faithfull@glasgow.ac.uk
* Correspondence: guiceg@cardiff.ac.uk; Tel.: +44-789-142-6510

check for updates

Abstract: The relative depletion of high field strength elements (HFSE), such as Nb, Ta and Ti, on normalised trace-element plots is a geochemical proxy routinely used to fingerprint magmatic processes linked to Phanerozoic subduction. This proxy has increasingly been applied to ultramafic-mafic units in Archaean cratons, but as these assemblages have commonly been affected by high-grade metamorphism and hydrothermal alteration/metasomatism, the likelihood of element mobility is high relative to Phanerozoic examples. To assess the validity of HFSE anomalies as a reliable proxy for Archaean subduction, we here investigate their origin in ultramafic rocks from the Ben Strome Complex, which is a 7 km^2 ultramafic-mafic complex in the Lewisian Gneiss Complex of NW Scotland. Recently interpreted as a deformed layered intrusion, the Ben Strome Complex has been subject to multiple phases of high-grade metamorphism, including separate granulite- and amphibolite-facies deformation events. Additional to bulk-rock geochemistry, we present detailed petrography, and major- and trace-element mineral chemistry for 35 ultramafic samples, of which 15 display negative HFSE anomalies. Our data indicate that the magnitude of HFSE anomalies in the Ben Strome Complex are correlated with light rare earth-element (LREE) enrichment likely generated during interaction with H_2O and CO_2-rich hydrothermal fluids associated with amphibolitisation, rather than primary magmatic (subduction-related) processes. Consequently, we consider bulk-rock HFSE anomalies alone to be an unreliable proxy for Archaean subduction in Archaean terranes that have experienced multiple phases of high-grade metamorphism, with a comprehensive assessment of element mobility and petrography a minimum requirement prior to assigning geodynamic interpretations to bulk-rock geochemical data.

Keywords: HFSE; rare earth-elements (REE); Archaean geodynamics; Lewisian Gneiss Complex; ultramafic-mafic complex; granulites; amphibolitisation; element mobility

1. Introduction

Geochemical fingerprinting, which commonly involves plotting immobile element ratios on bivariate and ternary diagrams, can aid discrimination between Phanerozoic tectonic environments [1–3]. One such proxy, which involves the relative depletion of high field strength-elements (HFSE; e.g., Nb, Ta, Zr, Hf and Ti) on normalised trace-element plots (Figure 1; herein referred to as the 'HFSE anomaly'), is commonly used to identify Phanerozoic arc magmas [4]. Despite being widely used as evidence for subduction-related magmatism, application of the HFSE anomaly requires caution, as it can also be generated by alternative mechanisms, such as crustal contamination [5] or via interaction with the sub-continental lithospheric mantle (SCLM; [6]). Moreover, several authors have demonstrated that the HFSE and rare earth-elements (REE), which are crucial for geochemical fingerprinting (as they are commonly assumed to be immobile), can be mobilised during some types of hydrothermal alteration and metasomatism [7–13], leading to further skepticism of HFSE anomalies as a reliable subduction proxy.
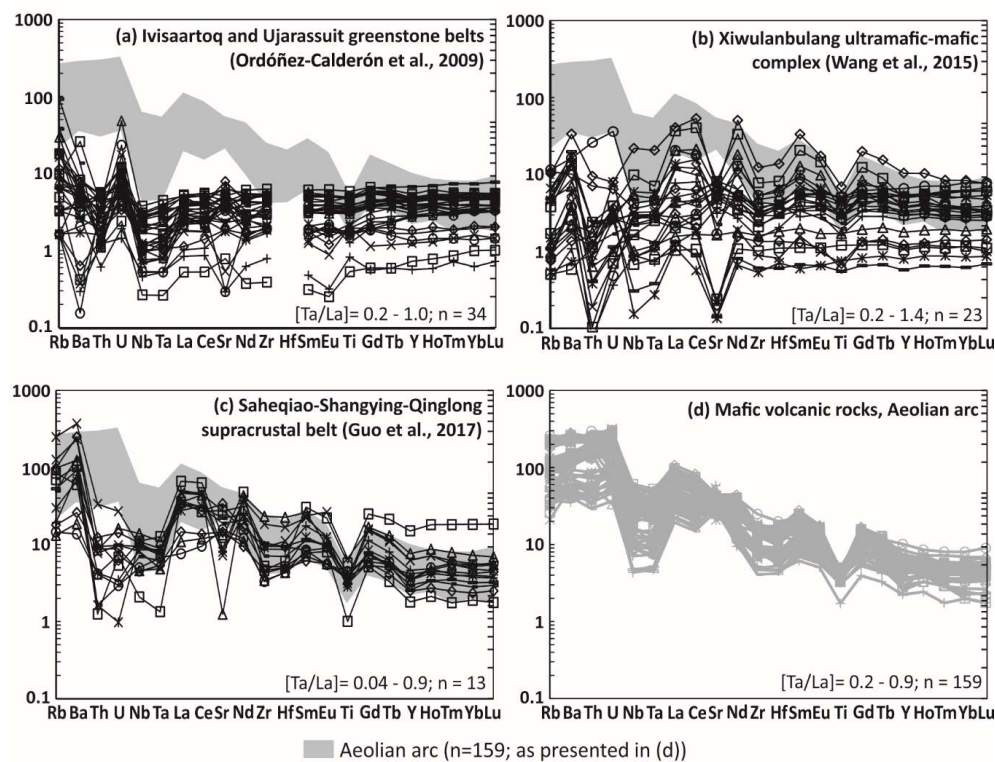
Figure 1. Primitive mantle-normalised trace-element plots comparing Archaean mafic rocks interpreted as the product(s) subduction-related magmatism (**a**–**c**) to mafic rocks from the Phanerozoic Aeolian arc [14–19], shown in (**d**).

Use of HFSE anomalies as supporting evidence for subduction-related magmatism has been extended to suites of mafic-ultramafic volcanic and/or plutonic rocks in several Archaean cratons over the last two decades [20–27]. Figure 1 details primitive mantle-normalised trace-element patterns for selected Archaean assemblages attributed to subduction-related magmatism in several Cratons. When compared with those from the Phanerozoic Aeolian arc, these Archaean examples often display relatively flat trace-element patterns and larger ranges in normalised abundances (as shown by Figure 1a,b), although other examples are more comparable to Phanerozoic patterns (e.g., Figure 1c). Given the implications that subduction-related interpretations have on Archaean geodynamic interpretations and the evolution of the early Earth, assessing the reliability of the HFSE anomaly as a viable fingerprint of Archaean subduction is of critical importance.

The Archaean geodynamics debate is primarily articulated around when and how modern-style plate tectonics—involving subduction and mid-ocean ridges in a globally linked system of internally rigid plates [28–30]—began on Earth [31–33]. Some authors argue that a form of the current geodynamic regime (of which modern-style subduction is a critical component) has been in operation since at least 3.6 Ga [31,34–38]. Others dispute such interpretations, maintaining that the distinctive geochemical signatures, lithological assemblages, structures and metamorphic imprints exhibited by cratons are incompatible with modern-style plate tectonics having operated during the Archaean [2,32,33,39,40]. Isolated or episodic subduction represents a component of some alternative geodynamic models for the Archaean Earth, which are numerous, with a stagnant lid geodynamic regime representing the end-member alternative to modern-style plate tectonics [32,41]. Alternatively, it has been suggested that a marked increase in the Rb/Sr ratios of juvenile continental crust at 3.0 Ga represents a transition from mafic-dominated to felsic-dominated continental crust as a result of the onset of modern-style plate tectonics [42]. Ultimately, there is no consensus regarding the onset of plate tectonics, with age predictions ranging from the late Hadean [43] to the Neoproterozoic [44].

To assess the validity of HFSE anomalies as a reliable proxy for Archaean subduction, we here examine the origin of those displayed by well constrained and characterised ultramafic samples from the Ben Strome Complex of the Lewisian Gneiss Complex (LGC). Located on the northwest Scottish mainland, the Ben Strome Complex is an ultramafic-mafic complex that covers 7 km^2 and has been subject to multiple phases of high-grade metamorphism. Although the precise age of the Ben Strome Complex is ambiguous, it has recently been interpreted as representing a deformed layered intrusion that was emplaced into tonalite-trondhjemite-granodiorite (TTG) gneiss between 3.0 and 2.7 Ga, with the ultramafic and mafic rocks representing metamorphosed cumulates [45]. In this paper, we present bulk-rock geochemistry, detailed petrography and mineral chemistry for a suite of ultramafic rocks, which, unlike local mafic, intermediate and felsic lithologies, have not experienced partial melting [45–47]. After discussing bulk-rock geochemical controls and the origin of the HFSE anomalies in the Ben Strome ultramafic rocks, we outline the implications for geochemical fingerprinting of ultramafic-mafic units in Archaean cratons and element mobility associated with high-grade metamorphism.

2. Regional Geology

2.1. The Mainland Lewisian Gneiss Complex

The mainland LGC is a ca. 125 × 25 km fragment of the North Atlantic Craton located in NW Scotland, west of the Moine Thrust, (Figure 2; [48]). Partially covered by Neoproterozoic to Ordovician sedimentary rocks, the mainland LGC predominantly comprises amphibolite- to granulite-facies TTG gneiss representing metamorphosed felsic magmatic rocks, with subordinate ultramafic, mafic and metasedimentary lithologies [49–51]. Further to being affected by polyphase, high-grade metamorphism, these lithologies are cross-cut by a suite of Palaeoproterozoic mafic dykes (known locally as the 'Scourie Dykes') and later pegmatitic sheets in some areas [48,49].

The mainland LGC is traditionally subdivided into a granulite-facies Central Region that is structurally bound by amphibolite-facies Northern and Southern Regions (Figure 2; [48,50]. Relative to the Northern and Southern Regions, the Central Region is geochemically depleted in Cs, Rb, Th, U and K [52], with this portion of the LGC previously interpreted as representing deeper crustal levels [53]. Alternative interpretations, which are largely based on geochronology, envisage the mainland LGC as comprising 6 terranes that have distinct magmatic and metamorphic histories [54–58]. Such interpretations remain controversial [59], although the Laxford Shear Zone is generally accepted as representing a significant crustal boundary (Figure 2; [60,61]). As a consequence, we use the traditional subdivision of Park and Tarney [53] in this paper.

While the stratigraphic and metamorphic history of the Central Region—within which the Ben Strome Complex is located (Figure 2)—remains a matter for considerable discussion, it is generally

accepted that the magmatic precursors to the TTG gneiss intruded between 3.05 and 2.80 Ga [54,62,63]. A granulite-facies tectonothermal event, which is known locally as the Badcallian and likely occurred between 2.8 and 2.7 Ga [62,64,65] (although some authors place it at 2.5–2.4 Ga [56]), led to widespread partial melting of the TTG gneisses and some mafic lithologies [46]. This event, for which peak P–T conditions have been estimated at 0.8–1.2 GPa, is characterised by a pervasive, shallow- to moderate-dipping gneissosity that displays open to isoclinal folds [51,62,64–67]. The Badcallian was succeeded by a granulite- to amphibolite-facies tectonothermal event known locally as the Inverian, which is expressed as localised, NW–SE-trending shear zones, but may have been more pervasive [51,56]. Although the precise extent of this event, which likely occurred between 2.5 and 2.4 Ga, is poorly constrained due to subsequent re-activation [68–71], it is defined as preceding the emplacement of the Scourie Dykes [72,73]. This NW–SE-trending suite of mafic dykes was largely intruded between 2.42 and 2.38 Ga, with individual dykes up to 100 m wide [72–74]. Between 1.9 and 1.5 Ga, the LGC was affected by a collection of greenschist- to amphibolite-facies metamorphic and magmatic events known as the Laxfordian [60,61,75]. In the Central Region, the Laxfordian typically manifests as roughly E–W-trending shear zones that are tens of metres wide and display a steeply dipping gneissosity that is markedly thinner than that of the Badcallian foliation [60,61].
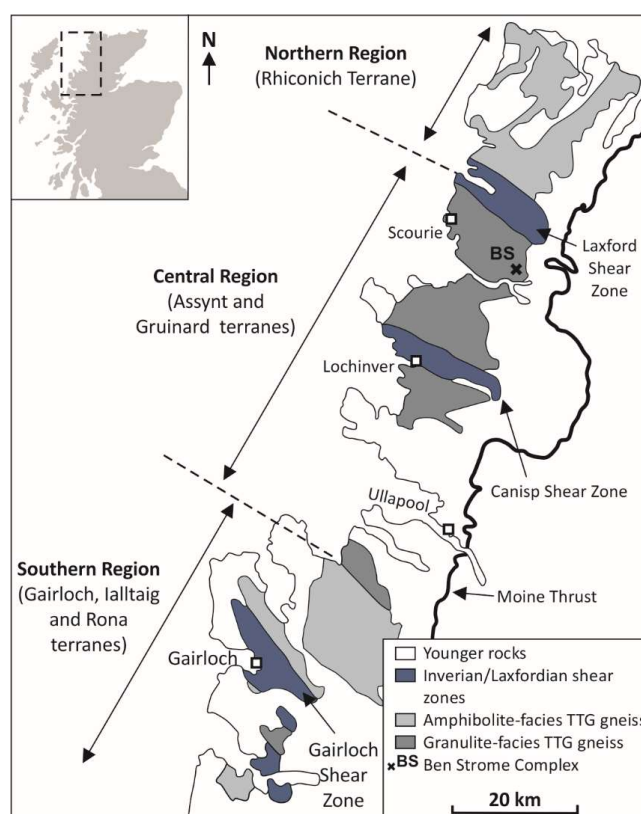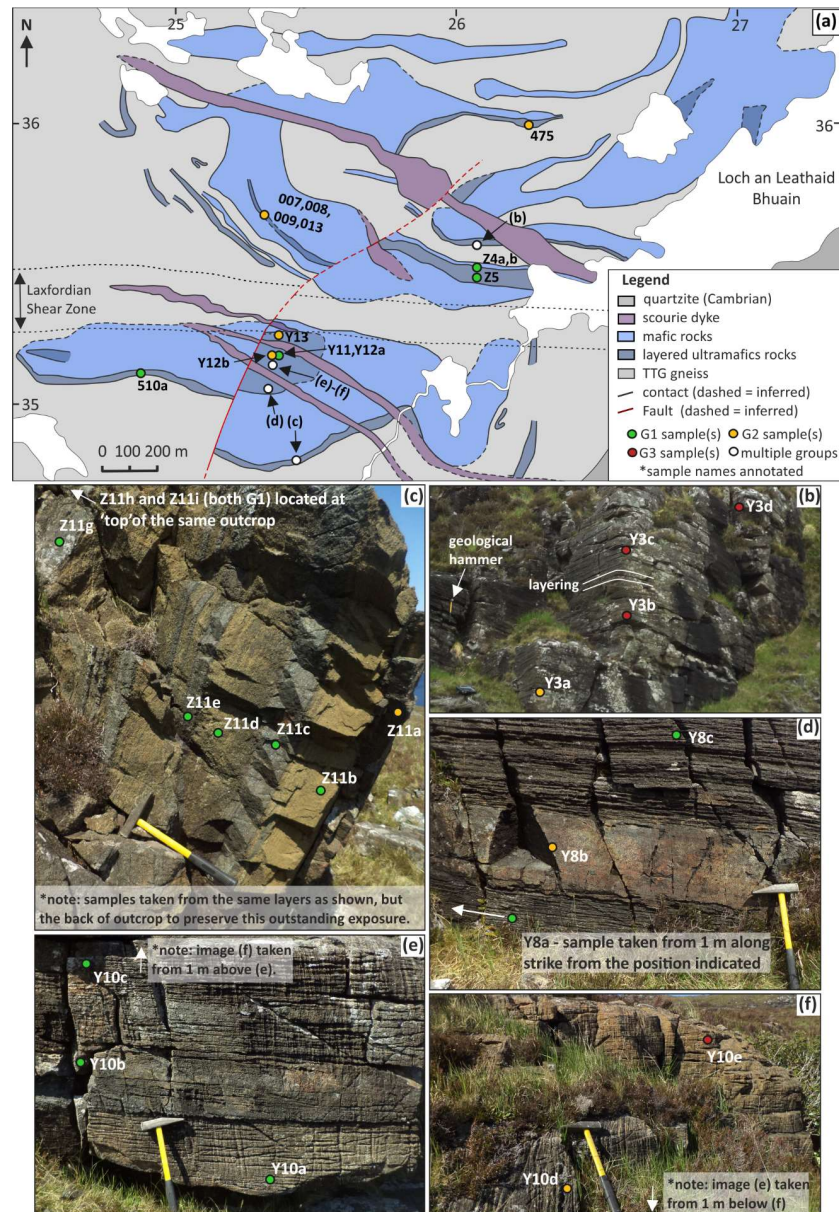

Figure 2. Simplified geological map of the Lewisian Gneiss Complex (LGC), including the location of the Ben Strome Complex. Redrawn after: [45,51,54,76]. Inset: location of the LGC in Scotland.

2.2. The Ben Strome Complex

The Ben Strome Complex (Figure 3)—located 13 km SE of the village of Scourie (Figure 2)—is one of several large ultramafic-mafic complexes to occur within the Central Region of the LGC [45,76–81]. The origin and geodynamic significance of such complexes has remained enigmatic since they were first described [49], with a wide-range of interpretations suggested, including: fragments of a pre-TTG (possibly oceanic) crust that was invaded by TTG magmas [79]; accreted oceanic crust [53]; the sagducted remnants of greenstone belts [76]; or, as proposed most recently, deformed layered

intrusion(s) emplaced into TTG gneiss [45]. Moreover, while the ultramafic-mafic rocks of the LGC have traditionally been regarded as sharing a common origin, [79], recent studies have suggested that the complexes may represent petrogenetically and/or temporally distinct phases of ultramafic-mafic Archaean magmatism [45,81].

Figure 3. (**a**) Simplified geological map of the Ben Strome Complex detailing the locations of samples used in this study (modified after Guice et al. [45]). Structural measurements and stereonet plots are detailed in Guice et al. [45]; (**b**–**f**) Field photographs detailing sample locations at specific outcrops marked on (**a**).

The 7 km^2 Ben Strome Complex, which represents the largest ultramafic-mafic complex in the LGC and has recently been subject to detailed characterisation by field mapping and observations [45], is truncated by a large Laxfordian shear zone and cross-cut by numerous Scourie Dykes (Figure 3). Approximately 70% of the Complex is composed of mafic rocks comprising metagabbro, garnet-metagabbro and amphibolite, with layered ultramafic rocks (predominantly metapyroxenite, with subordinate metaperidotite) comprising the remainder (Figure 3; [45]). These ultramafic portions, which are typically 5 to 50 m in stratigraphic thickness and persist for hundreds of metres along strike,

preserve systematic layering typical of layered intrusions [45]. The mafic portions of the Complex are characterised by sporadic lithological heterogeneity on a scale of centimetres to tens of metres, with subtle remnants of primary layering rarely preserved [45]. These portions of the Complex display evidence for partial melting of mafic lithologies in the form of cross-cutting plagioclase-rich and pyroxene-bearing leucosomes [45,46]. Moreover, prior to Scourie Dyke emplacement, the Ben Strome Complex was subject to polyphase folding and granulite-facies metamorphism [45].

3. Materials and Methods

We present petrography and geochemical data for 35 ultramafic samples from the Ben Strome Complex. Of these samples, 18 are from north of the Laxfordian shear zone and 17 are from south of the shear zone (Figure 3). Seven of the samples correspond to the spinel mineral chemistry samples reported by Guice et al. [45]. The locations of the samples within the Ben Strome Complex are detailed in Figure 3, with GPS coordinates provided in Table 1. All 35 samples were analysed for bulk-rock major and trace-element chemistry, and polished thin sections of 33 of these samples were made at Cardiff University for further petrological analysis. Further to optical microscopy, thin sections were subject to detailed petrographic assessment by element mapping on an analytical scanning electron microscope (A-SEM) at Cardiff University. Major-element mineral chemistry was collected for 17 thin sections, with accompanying trace-element mineral chemistry carried out on a subset of 8 thin sections by laser ablation-inductively couple plasma-mass spectrometry (LA-ICP-MS).

Table 1. Location and modal mineralogy for each sample.

Thin Section	Grid Reference	Modal Mineralogy (%)							
		EM	ol	ser	opx	cpx	amf	spn	carb
Group 1 samples									
Lw16-Y8a	NC25333/35066	Y	0.0	0.0	58.1	23.5	16.4	2.0	
Lw16-Y8c	NC25333/35066	Y	0.9	16.5	29.0	44.8	8.2	0.7	
Lw16-Y10a	NC25340/35130	Y	0.0	44.1	28.3	18.6	9.1	0.0	Y
Lw16-Y10b	NC25340/35130	Y	0.0	0.0	49.9	19.1	29.2	1.8	
Lw16-Y10c	NC25340/35130	Y	5.0	2.0	57.0	12.8	22.5	0.8	
Lw16-Y11	NC25328/35174	Y	0.0	0.0	40.3	44.9	12.3	2.6	
Lw16-Y12a	NC25323/35182	Y	2.8	23.3	30.8	27.0	15.2	0.8	
Lw16-Z4a	NC26037/35434		0.0	0.0	46.0	3.0	48.0	3.0	
Lw16-Z4b	NC26041/35444	Y	0.4	54.8	12.9	5.3	26.7	0.0	Y
Lw16-Z5	NC26066/35466		3.0	55.0	4.0	8.0	28.5	1.5	
Lw16-Z11b	NC26072/35569		2.0	82.0	10.0	0.0	6.0	0.0	
Lw16-Z11c	NC26072/35569	Y	0.0	0.0	42.2	25.0	28.3	4.4	
Lw16-Z11d	NC26072/35569	Y	0.0	77.0	0.0	22.3	0.0	0.8	
Lw16-Z11e	NC26072/35569	Y	0.0	0.0	0.9	17.5	77.9	3.8	Y
Lw16-Z11g	NC26072/35569	Y	0.0	0.0	47.2	3.3	44.3	5.1	
Lw16-Z11h	NC26072/35569		0.0	0.0	58.0	10.0	28.0	4.0	
Lw16-Z11i	NC26072/35569	Y	0.0	70.0	0.0	24.6	2.7	2.7	
Lw16-510a	NC24879/35120	Y	0.0	2.7	38.2	0.0	57.8	1.4	
Group 2 samples									
Lw16-Y3a	NC25439/34795	Y	0.0	59.2	0.5	28.9	11.0	0.5	Y
Lw16-Y8b	NC25333/35066	Y	0.0	1.0	47.1	22.6	27.3	2.1	Y
Lw16-Y12b	NC25323/35182		0.0	0.0	36.0	4.0	59.0	1.0	
Lw16-Y13	NC25345/35234	Y	3.9	12.7	31.4	36.9	14.6	0.4	Y
Lw16-475	NC26263/35986	Y	1.7	36.6	10.0	9.1	41.6	0.4	Y
Lw16-Y10d	NC25340/35130	Y	0.0	78.8	8.8	9.0	0.1	3.4	Y
Lw16_Z11a	NC26072/35569	Y	0.0	30.7	0.0	20.1	49.2	0.0	Y
LEW007	NC25375/35591	Y	0.7	66.5	5.3	26.5	1.0	0.0	Y
LEW008	NC25375/35591		0.0	0.0	91.0	0.0	9.0	0.0	Y
LEW009	NC25375/35591	Y	3.0	51.0	4.0	35.0	5.0	0.0	Y
LEW013	NC25228/35666	Y	0.5	70.5	16.0	2.0	8.0	3.0	Y

Table 1. *Cont.*

Thin Section	Grid Reference	Modal Mineralogy (%)							
		EM	ol	ser	opx	cpx	amf	spn	carb
Group 3 samples									
Lw16-Y3b	NC25439/34795	Y	5.2	9.1	45.6	0.0	39.7	0.4	Y
Lw16-Y3c	NC25439/34795	Y	0.0	2.4	37.6	4.6	54.8	0.0	Y
Lw16-Y3d	NC25439/34795	Y	0.0	45.8	5.6	43.1	4.3	1.1	Y
Lw16-Y10e	NC25328/35174	Y	0.0	100.0	0.0	0.0	0.0	0.0	Y
Group averages									
Group 1	*n* = 18		1	24	31	17	26	2	
Group 2	*n* = 11		1	37	23	18	21	1	
Group 3	*n* = 4		1	39	22	12	25	0	

Abbreviations: ol = olivine; ser = serpentine; opx = orthopyroxene; cpx = clinopyroxene; amf = amphibole; spn = spinel; carb = carbonate; EM = element map; Y = yes.

3.1. Bulk-Rock Chemistry

Samples were crushed in a Mn steel jaw-crusher and subsequently ground to a fine powder in an agate ball mill, before loss on ignition (LOI) was determined gravimetrically. A sample mass of 0.1 g was accurately weighed and mixed with 0.6 g of Claisse 50:50 Li metaborate Li tetraborate flux in a Claisse BIS! Pt-Rh crucible [82]. Approximately 0.5 mL of a Li iodide solution was added as a non-wetting agent [82], before the mixture was fused over a propane burner on a Claisse FLUXY (automated) fusion system. The mixture was subsequently poured into a Teflon beaker containing 50 mL of 4% HNO_3, where it was dissolved using a magnetic stirrer [82]. Following dissolution of all glass fragments, the solution was spiked with 1 mL of a 100 ppm Rh spike solution (for use as an internal standard) and made up to 100 mL with 18.2 MΩ deionised water [82]. Samples were subsequently analysed for major and trace elements using inductively coupled plasma optical emission spectrometry (ICP-OES) and inductively coupled plasma mass spectrometry (ICP-MS) respectively. Details of the analytical procedure can be found in McDonald and Viljoen [82]. Accuracy was constrained by analysis of the following international reference materials prepared by the Geological Survey of Japan and University of Durham [83–85]: JB1a, JP1, JG1A, JA2, JG3, BIR-1, SD01, NIM-P, GP13 and MRG1. Precision was constrained by conducting duplicate analyses of 10% of samples and by repeat analysis of international reference material JP1 (see Supplementary Material—Table S1). Standards and blanks were prepared and analysed using the methodology and instrumentation described above, with the sample material omitted for blanks.

3.2. Element Mapping

Detailed petrographic assessment by element mapping used a Zeiss Sigma HD Field Emission Gun A-SEM equipped with two Oxford Instruments 150 mm^2 Energy Dispersive X-ray Spectrometry (EDS) detectors at the School of Earth and Ocean Sciences, Cardiff University. Operating conditions were set at 20 kV and aperture size to 120 µm, with a nominal beam current of 4 nA and working distance of 8.9 mm. Using Aztec software, maps were acquired at 100 to 150× magnifications, with resulting pixel sizes ranging from 10 to 22 µm, depending on the resolution of acquired spectral images. A process time of 1 µs was used in conjunction with a pixel dwell time of 3000–6000 µs. Element maps were then background correlated and element overlaps deconvolved using Aztec software, before modal mineralogy was calculated from relative element concentrations using the analyse phases algorithm in Aztec. Boundary tolerance and grouping level were set at 2 and 1 respectively, with any unassigned pixels discarded from the modal mineralogy. Table 1 details the modal mineralogy of assessed samples and highlights those that were subject to element mapping.

3.3. Major-Element Mineral Chemistry

Major-element mineral chemistry was conducted using the same A-SEM as described in Section 3.2. Operating conditions were set at 20 kV and aperture size to 60 µm, with analytical drift checks carried

out every 20 min using a Co reference standard. A suite of standards from ASTIMEX and Smithsonian were used to calibrate the EDS analyser and perform secondary standard checks every hour. In total, analyses of 366 orthopyroxene grains were conducted, alongside analyses of 152 clinopyroxene grains, 188 amphibole grains (originally published in the Supplementary Material of Guice et al. [45]), 70 olivine grains, and 94 serpentine grains. The Fe^{2+} and Fe^{3+} was calculated stoichiometrically [86] and the full dataset, including information on which thin sections were analysed, is available in the Supplementary Material (Table S2).

3.4. Trace-Element Mineral Chemistry

LA-ICP-MS was carried out using a New Wave Research UP213 UV laser system and attached Thermo X Series 2 ICP-MS at Cardiff University. Line analyses were used, with a minimum line length of 300 µm and beam diameter of 80 µm. Samples were analysed using an acquisition time of between 90 and 410 s, with a 20-s gas blank and 10-s wash out. Calibration of the ICP-MS was achieved using United States Geological Survey (USGS) basalt glass standards BIR-1g, BHVO-2g and BCR-2g. For silicate mineral phases, Si concentrations (as determined using the A-SEM method described above) were used as an internal standard, with Ca concentrations used as an internal standard for carbonate mineral phases. Further details of the analytical procedure and analytical isotopes are given in Hughes et al. [87]. Analyses of 46 orthopyroxene grains were conducted, alongside analyses of 40 clinopyroxene grains and 77 amphibole grains, with the full dataset available in the Supplementary Material (Table S3). In addition, 7 calcite grains were analysed, although some silicate material was included in the ablation process due to the small size (µm-scale) and morphology of these grains, which are often intergrown with silicate minerals. Individual analyses record SiO_2 values of between 2.5 and 15.1 wt. %, with this dilution of the pure carbonate signature taken into consideration in the discussion of the results.

4. Bulk-Rock Chemistry

Based on trace-element geochemistry, the ultramafic rocks of the Ben Strome Complex are here subdivided into 3 groups, with distinctive patterns on chondrite-normalised REE and primitive mantle-normalised trace-element plots (Figure 4). These geochemical groups are best defined using chondrite-normalised Ce/Yb ratios, with group 1 samples (*n* = 20) displaying values of between 0.6 and 1.4, group 2 samples (*n* = 11) showing values of between 1.6 and 12.8, and group 3 samples (*n* = 4) exhibiting values of between 15.6 and 34.9 (Figure 4). On primitive mantle-normalised trace-element plots (Figure 4), the group 1 samples display largely flat patterns ([La/Nb]$_N$ = 0.2–2.5), while group 2 samples show negative Nb-Ta anomalies ([La/Nb]$_N$ = 0.8–34.8), and group 3 samples exhibit negative Nb-Ta-Zr-Hf-Ti anomalies ([La/Nb]$_N$ = 13.1–43.1).
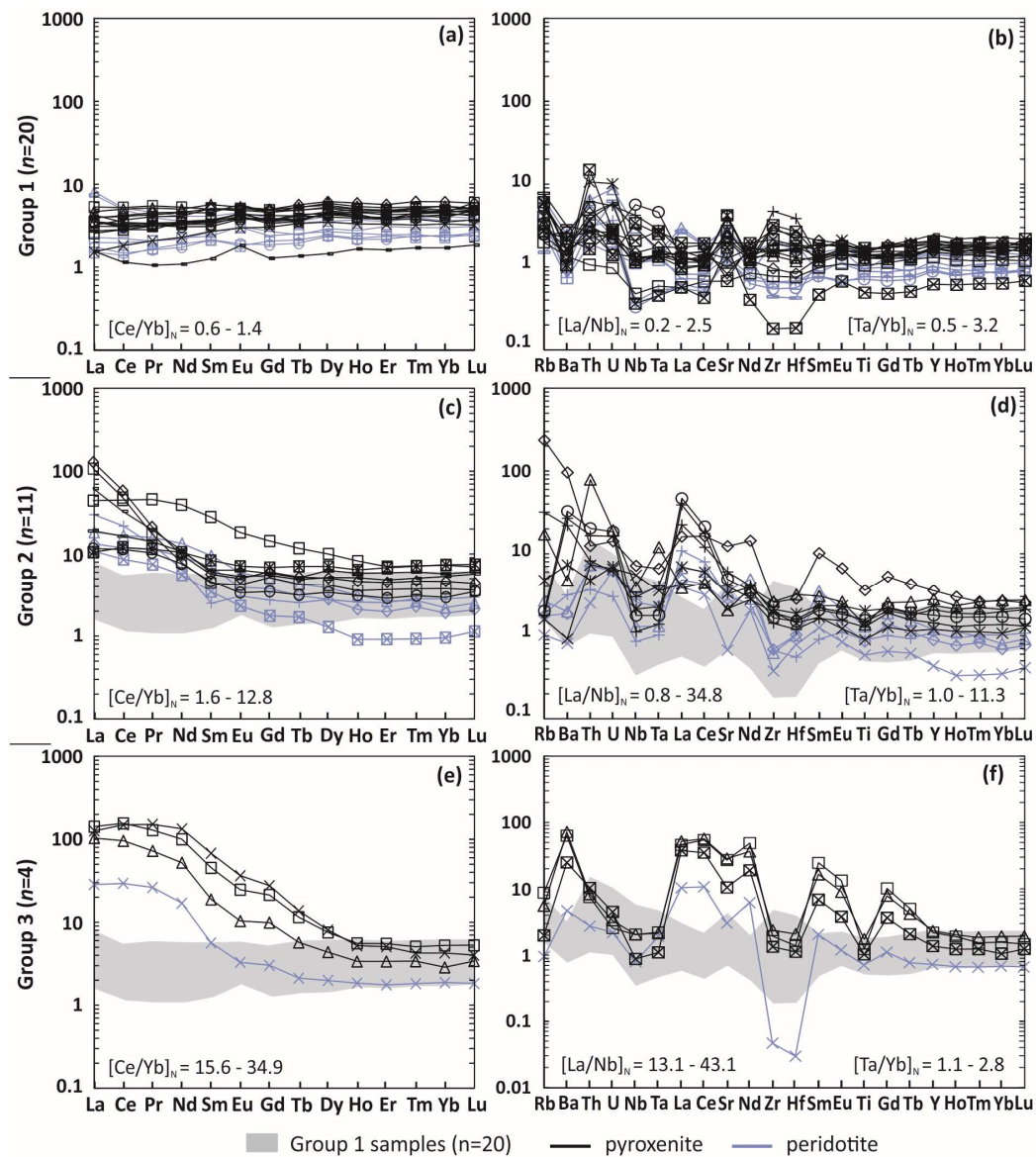
Figure 4. Chondrite-normalised Rare Earth Elements (REE) plots and primitive mantle-normalised trace-element plots for the group 1 (**a**,**b**), group 2 (**c**,**d**) and group 3 (**e**,**f**) ultramafic rocks from the Ben Strome Complex. Normalised values from McDonough and Sun [88]. Note scale change on (**f**).

4.1. Spatial Distribution of Samples

Group 1 and 2 samples are numerous throughout the Ben Strome Complex, occurring to the north and south of the E–W-trending Laxfordian shear zone (Figure 3a). Group 3 samples exclusively occur to the south of the large Laxfordian shear zone (Figure 3a), with 3 of the samples present in one, 6-m thick package of ultramafic rocks on the southern edge of the Complex (Figure 3b). Although stratigraphically thick (>3 m) sequences of ultramafic rocks often contain several samples belonging to the same geochemical group (Figure 3c), samples from different geochemical groups are often located less than 1 m (stratigraphically) from one another (Figure 3b–f). In the case of Figure 3d, two group 1 samples (Y8a and Y8c), which exhibit flat REE patterns and no HFSE anomalies, are located less than 0.3 m (stratigraphically) above and below a group 2 sample (Y8b), which displays LREE enrichment and negative Nb-Ta anomalies (Figure 4a–d). Similarly, in the case of Figure 3e–f, three group 1 samples (Y10a–c) are located ~1 m (stratigraphically) below a group 2 sample (Y10d), which is located less than 0.5 m below a group 3 sample (Y10e).

4.2. Major-Elements

The three geochemical groups cannot be distinguished by major-element geochemistry, with major-element bivariate plots (Figure 5) demonstrating that MgO in the Ben Strome ultramafic rocks displays moderate negative correlations with SiO_2, TiO_2, Al_2O_3, CaO and Na_2O, a moderate positive correlation with NiO ($R^2 = 0.5$–0.6), and no correlation with Fe_2O_3 or Cr_2O_3 ($R^2 \leq 0.1$). These plots (Figure 5) also include the compositional ranges of silicate minerals from the Ben Strome Complex, demonstrating that the bulk-rock major-element compositions of the analysed rocks are essentially a function of modal mineral abundances. The major-element data are presented on a volatile-free basis in Figure 5, with summaries of each geochemical group included in Table 2 and the full dataset available in the Supplementary Material (Table S1).
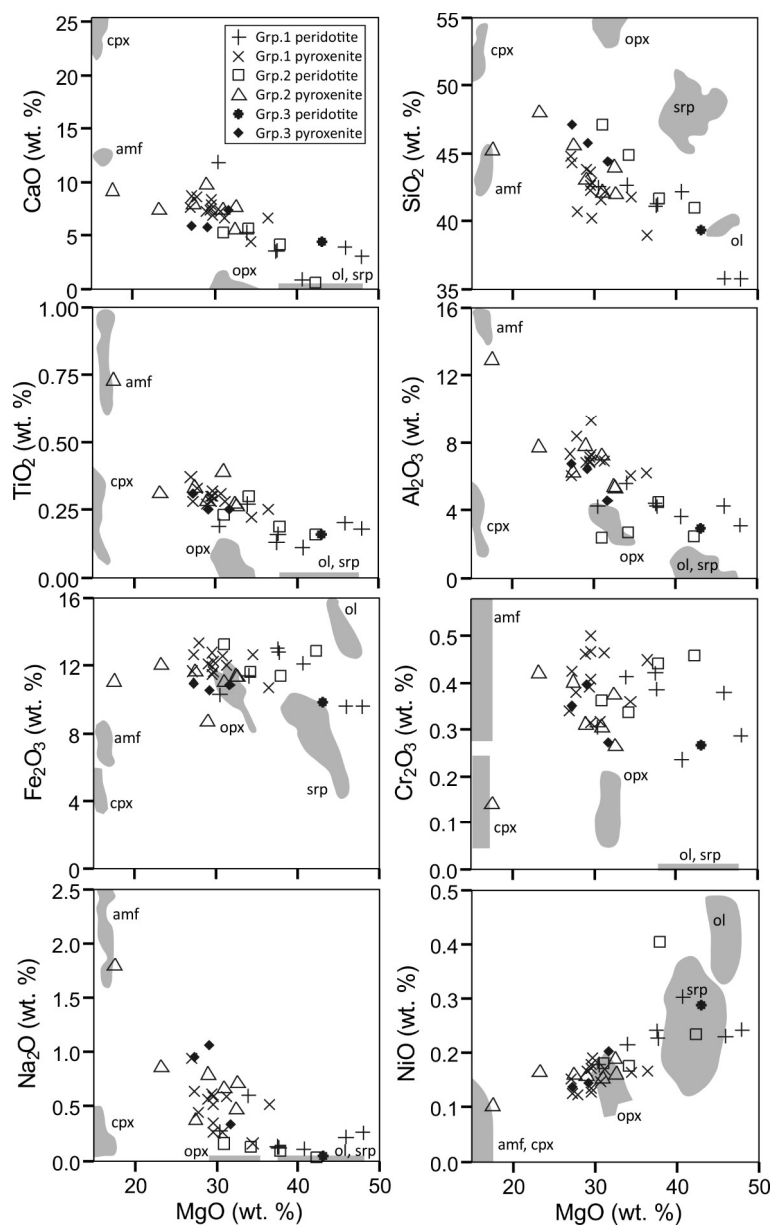
Figure 5. Bivariate plots detailing the major and minor element compositions of the Ben Strome samples, with grey mineral chemistry field included for reference. Note: amphibole fields are after Guice et al. [45]. Abbreviations: amf = amphibole; cpx = clinopyroxene; ol = olivine; opx = orthopyroxene; srp = serpentine.

Table 2. Representative bulk-rock analyses of ultramafic rocks from the Ben Strome Complex. Major-element analyses conducted using inductively coupled plasma optical emission spectrometry (ICP-OES). Trace-element analyses conducted using inductively coupled plasma mass spectrometry (ICP-MS). The full dataset is included in the Supplementary Material (Table S1).

	Group 1 (*n* = 20)				Group 2 (*n* = 11)				Group 3 (*n* = 4)			
	Min	Max	Mean	SD *	Min	Max	Mean	SD *	Min	Max	Mean	SD *
Major elements (wt. %)												
SiO_2	35.8	44.8	41.6	2.3	41.0	48.0	43.9	2.2	39.4	47.1	44.1	2.9
TiO_2	0.1	0.4	0.3	0.1	0.2	0.7	0.3	0.1	0.2	0.3	0.2	0.1
Al_2O_3	3.1	9.3	6.1	1.6	2.4	12.8	5.9	2.9	3.0	6.8	5.1	1.5
Fe_2O_3	9.6	13.4	11.8	1.0	8.7	13.3	11.44	1.1	9.9	11.0	10.6	0.4
MnO	0.1	0.3	0.2	0.0	0.1	0.2	0.2	0.0	0.2	0.2	0.2	0.0
MgO	27.0	47.9	33.3	5.9	17.5	42.2	31.0	6.4	27.2	43.0	32.8	6.1
CaO	0.9	11.9	6.4	2.5	0.6	9.7	6.3	2.5	4.4	7.4	5.9	1.1
Na_2O	0.1	0.9	0.4	0.2	0.03	1.8	0.6	0.5	0.1	1.1	0.6	0.4
K_2O	0.01	0.1	0.06	0.0	0.01	1.35	0.2	0.4	0.01	0.4	0.2	0.2
P_2O_5	0.01	0.04	0.02	0.0	0.01	0.04	0.02	0.0	0.01	0.04	0.02	0.0
LOI	0.8	9.4	3.9	n/a	0.7	8.2	4.6	n/a	1.9	7.5	4.0	n/a
Trace elements (ppm)												
Sc	13.3	32.9	23.8	21.2	10.8	33.8	24.3	5.7	7.1	25.7	19.1	7.4
V	82.2	201.4	126.1	36.1	36.0	165.9	101.0	39.4	56.0	116.1	91.6	39.4
Cr	1577	3475	2697	446.8	1077	3165	2401	596.3	1787	2612	2161	344.7
Co	81.2	108.0	95.6	8.3	70.6	113.8	95.3	21.2	86.0	110.2	97.6	8.7
Ni	929	2350	1419	353.5	832	3236	1492	596.7	1079	2357	1532	515.9
Cu	3.5	445.2	67.4	93.8	4.8	118.3	42.1	31.6	4.9	393.8	133.5	157.0
Zn	56.5	1756	169	364.5	31.7	165.2	69.3	43.3	73.4	97.9	83.5	9.6
Ga	3.3	7.9	6.2	1.4	3.6	14.7	6.4	3.1	3.2	8.1	5.7	1.8
Rb	0.9	51.1	2.6	1.1	0.6	141.1	16.5	39.8	0.6	5.2	2.6	1.8
Sr	13.5	84.0	42.0	21.6	13.4	245.9	80.3	58.9	60.7	568.1	343.9	216.0
Y	2.7	10.5	6.7	2.0	1.9	15.3	80.6	3.7	3.1	9.9	7.1	2.8
Zr	1.9	49.4	17.5	11.4	4.0	27.4	15.7	8.0	0.5	24.9	14.9	9.2
Nb	0.2	3.7	1.2	0.9	0.6	4.7	1.9	1.2	0.5	1.4	1.0	0.4
Cs	0.1	1.4	0.7	0.4	0.2	4.4	0.8	1.2	0.2	0.3	0.3	0.0
Ba	4.9	20.8	11.4	4.4	5.4	634.4	119.0	176.3	31.0	474.2	271.5	181.2
La	0.4	1.9	0.8	0.4	2.5	30.4	9.8	6.8	6.7	33.6	23.7	10.3
Ce	0.7	3.2	2.0	0.8	5.3	35.7	15.7	8.1	18.0	95.1	18.0	31.0
Pr	0.1	0.5	0.3	0.1	0.7	4.4	1.6	0.9	2.4	14.0	8.8	4.5
Nd	0.5	2.4	1.5	0.5	2.5	18.0	5.5	4.1	7.8	61.0	34.6	20.4
Sm	0.2	0.8	0.5	0.2	0.4	4.1	1.2	1.0	0.8	10.0	5.1	3.5
Eu	0.1	0.3	0.2	0.1	0.1	1.0	0.3	0.2	0.2	2.1	1.1	0.7
Gd	0.3	1.0	0.7	0.2	0.4	2.9	1.1	0.6	0.6	5.5	3.1	1.9
Tb	0.1	0.2	0.1	0.0	0.1	0.4	0.2	0.1	0.1	0.5	0.3	0.2
Dy	0.4	1.5	1.0	0.3	0.3	2.5	1.2	0.6	0.5	2.0	1.4	0.6
Ho	0.1	0..3	0.2	0.1	0.1	0.5	0.2	0.1	0.1	0.3	0.2	0.1
Er	0.3	0.9	0.6	0.2	0.2	1.1	0.6	0.3	0.3	0.9	0.6	0.2
Tm	0.04	0.2	0.1	0.0	0.02	0.2	0.1	0.0	0.04	0.1	0.1	0.0
Yb	0.3	1.0	0.6	0.2	0.2	1.2	0.7	0.3	0.3	0.8	0.6	0.2
Lu	0.1	2.0	0.1	0.0	0.03	0.2	0.1	0.0	0.1	0.1	0.1	0.0
Hf	0.1	1.1	0.4	0.2	0.2	0.9	0.4	0.2	0.01	0.6	0.3	0.2
Ta	0.02	0.2	0.1	0.0	0.04	0.4	0.1	0.1	0.04	0.1	0.07	0.0
Pb	0.5	7.3	3.2	1.9	1.4	5.1	3.0	2.7	3.0	9.0	5.3	2.3
Th	0.1	1.2	0.3	0.3	0.2	6.3	1.2	1.7	0.2	0.8	0.6	0.2
U	0.02	0.2	0.1	0.1	0.1	0.4	0.2	0.1	0.04	0.1	0.06	0.0

* SD = standard deviation.

4.3. Trace-Elements

The group 1 samples exhibit flat patterns ($[Ce/Yb]_N$ = 0.6–1.4) on chondrite-normalised REE plots (Figure 4a), with REE concentrations ranging from 1.1 to 8.1× chondrite. Peridotite samples show slightly lower absolute REE abundances than pyroxenite samples but display parallel patterns (Figure 4a). On the primitive mantle-normalised trace-element plot (Figure 4b), the group 1 samples exhibit relatively flat patterns ($[Ta/Yb]_N$ = 0.6–3.2) punctuated by positive Th, U and Rb

anomalies. A key feature is that there are no negative HFSE anomalies ([La/Nb]$_N$ = 0.2–2.4) on these trace-element plots.

The group 2 samples exhibit moderate LREE enrichment ([Ce/Yb]$_N$ = 1.6–12.8), negatively sloping LREE patterns ([La/Nd]$_N$ = 1.0–13.5) and flat heavy-REE (HREE) on chondrite-normalised plots (Figure 4c), with normalised REE values ranging from 0.9 to 128.1. Peridotite samples show slightly lower absolute REE abundances relative to pyroxenite samples, but the patterns are parallel (Figure 4d). On the primitive mantle-normalised plot (Figure 4d), the group 2 samples exhibit distinctive negative Nb-Ta anomalies ([La/Nb]$_N$ = 0.8–34.8), LREE enrichment and positive Th-U anomalies. Notably, the [Ta/Yb]$_N$ ratios are generally comparable to those of the group 1 samples ([Ta/Yb]$_N$ = 1.0–4.4), although one sample displays a ratio of 11.3.
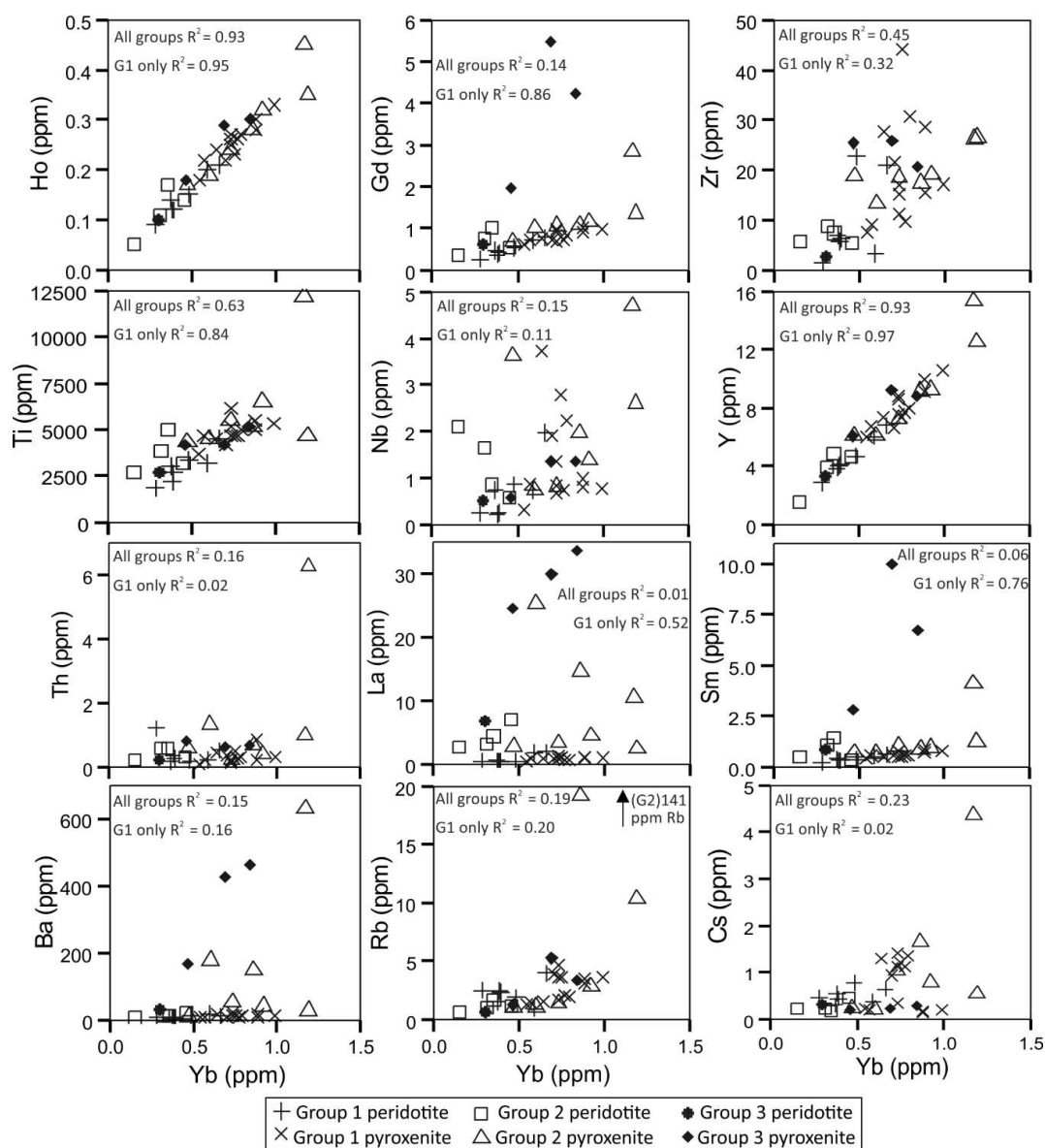
Figure 6. Bivariate plots detailing the trace-element compositions of the Ben Strome samples.

On the chondrite-normalised REE plot (Figure 4e), the group 3 samples exhibit strong LREE enrichment ([Ce/Yb]$_N$ = 15.6–34.9) and REE values ranging from 1.8 to 155.2× chondrite, with the peridotite samples relatively depleted in all REE relative to pyroxenite samples. On the primitive mantle-normalised plot (Figure 4f), the group 3 samples show distinctive negative Nb-Ta-Zr-Hf-Ti

anomalies ([La/Nb]$_N$ = 13.1–43.1), LREE enrichment, and positive Ba and Th anomalies. Notably, the normalised Ta/Yb ratios are comparable to both group 1 and 2 samples ([Ta/Yb]$_N$ = 1.1–2.8).

As shown by trace-element bivariate plots (Figure 6), Yb (a relatively immobile trace-element) displays strong positive correlations with Ho, Y and Ti (R^2 ≥ 0.6), moderate positive correlations with Zr (R^2 = 0.45), weak correlations with Nb, Th, Gd, Rb, Cs and Ba (R^2 = 0.1–0.3) and no correlation with La and Sm (R^2 ≤ 0.1) in the Ben Strome ultramafic rocks collectively. Although the relationship between Yb and other trace-elements in the group 1 samples is generally comparable to the other geochemical groups (Figure 6), these samples display a moderate to strong correlation between Yb and the LREE (Figure 6; R^2 = 0.5–0.8).

5. Petrography

As described by Guice et al. [45], the ultramafic rocks of the Ben Strome Complex comprise serpentine, olivine, orthopyroxene, clinopyroxene and spinel in variable proportions (Figure 7; Table 1), with rare sulphide minerals (pentlandite, pyrite, chalcopyrite and pyrrhotite) also present. All three geochemical groups contain a combination of metapyroxenite and metaperidotite lithologies, with each group displaying large ranges in the modal mineral abundances of silicate and oxide minerals. Table 1 details the modal mineral abundances of every thin section assessed in this study, alongside averages for each of the geochemical groups. These data demonstrate that there is no systematic variation in the modal abundances of silicate/oxide mineral phases between the 3 geochemical groups.

Olivine is almost entirely pseudomorphed by serpentine and minor magnetite, with olivine remnants only preserved in some thin sections (Table 1; Figure 7). Clinopyroxene is variably rimmed, replaced and veined by secondary amphibole on all scales, with only anhedral clinopyroxene remnants preserved within amphibole in some thin sections (Figure 7e,f). Such replacement can likely be attributed to polyphase amphibolitisation, with the Ben Strome Complex having experienced at least 2 distinct phases of amphibolite-facies metamorphism (during the ~2.5 Ga Inverian and 1.9–1.6 Ga Laxfordian events). Specific textures are not unique to individual geochemical groups, although clinopyroxene grains appear most intensely amphibolitised in group 2 and 3 samples, with amphibole veins commonly observed on the μm-scale (Figures 7 and 8).

Further to silicate, oxide and sulphide mineral phases, selected samples contain carbonate mineral phases (dolomite and calcite) in trace amounts (<0.2 modal %; Figure 8). Such carbonates display a range of mineralogical associations, occurring as: <0.2 mm wide calcite veins that cross-cut all mineral phases in individual thin sections (Figure 8a); <0.1 mm wide calcite veins within amphibole (Figure 8b); <0.8 mm diameter calcite grains within amphibole (Figure 8c); and <1 mm dolomite 'clots' within a serpentinite (Figure 8d). Carbonate minerals are extremely rare in the group 1 samples, with discontinuous veins (<0.1 mm wide) occurring in 3 out of 19 samples. In contrast, carbonate mineral phases are identified in 10 out of 11 group 2 thin sections, occurring as: <0.2 mm wide calcite veins through entire thin sections (Figure 8a); and <0.1 mm wide veins in amphibole (Figure 8b). Similarly, such phases are identified in all group 3 samples (*n* = 4), occurring, as: <0.2 mm wide veins in amphibole (Figure 8b); and μm-scale grains in amphibole and serpentine (Figure 8c,d).

The sulphide mineral assemblages displayed by the Ben Strome ultramafic rocks show systematic variation between the 3 geochemical groups. Group 1 samples contain extremely fine-grained (<50 μm diameter) pentlandite that is distributed relatively evenly throughout the thin sections (Figure 9a). Group 2 samples also contain fine-grained (<50 μm diameter) pentlandite, but also show rarer occurrences of coarser-grained (<150 μm diameter) pyrite (Figure 9b). Additional to fine-grained (<50 μm diameter) pentlandite, group 3 samples also contain frequent occurrences of coarse-grained (<500 μm diameter) pyrite (Figure 9c).
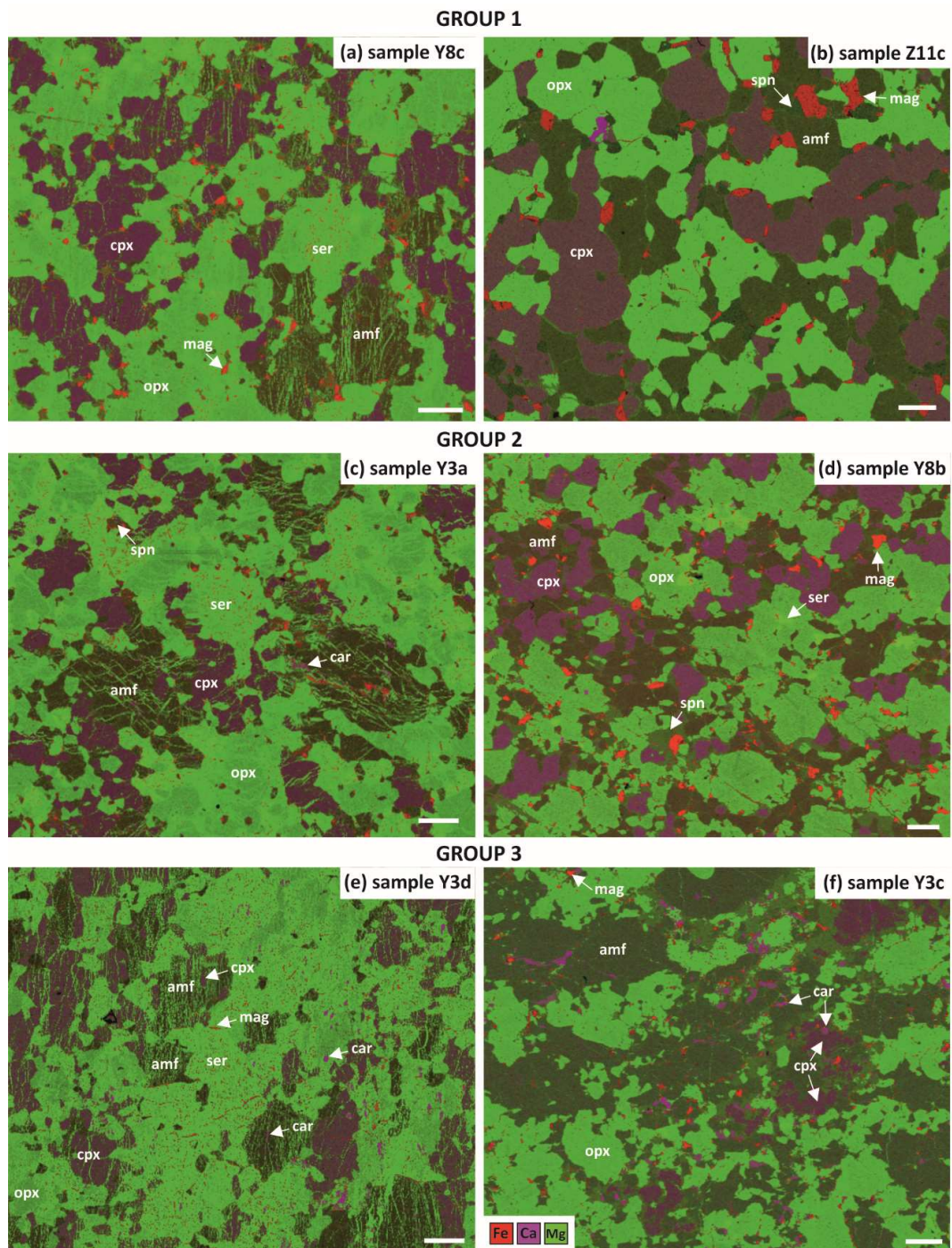
Figure 7. Element maps detailing the petrographic and textural characteristics of the Ben Strome ultramafics. (**a**,**b**) group 1 samples; (**c**,**d**) group 2 samples; (**e**,**f**) group 3 samples. Note the comparable textures between the geochemical groups. White scale bar = 1 mm. Abbreviations: amf = amphibole; car = carbonate phases; cpx = clinopyroxene; mag = magnetite; opx = orthopyroxene; ser = serpentine; spn = spinel.
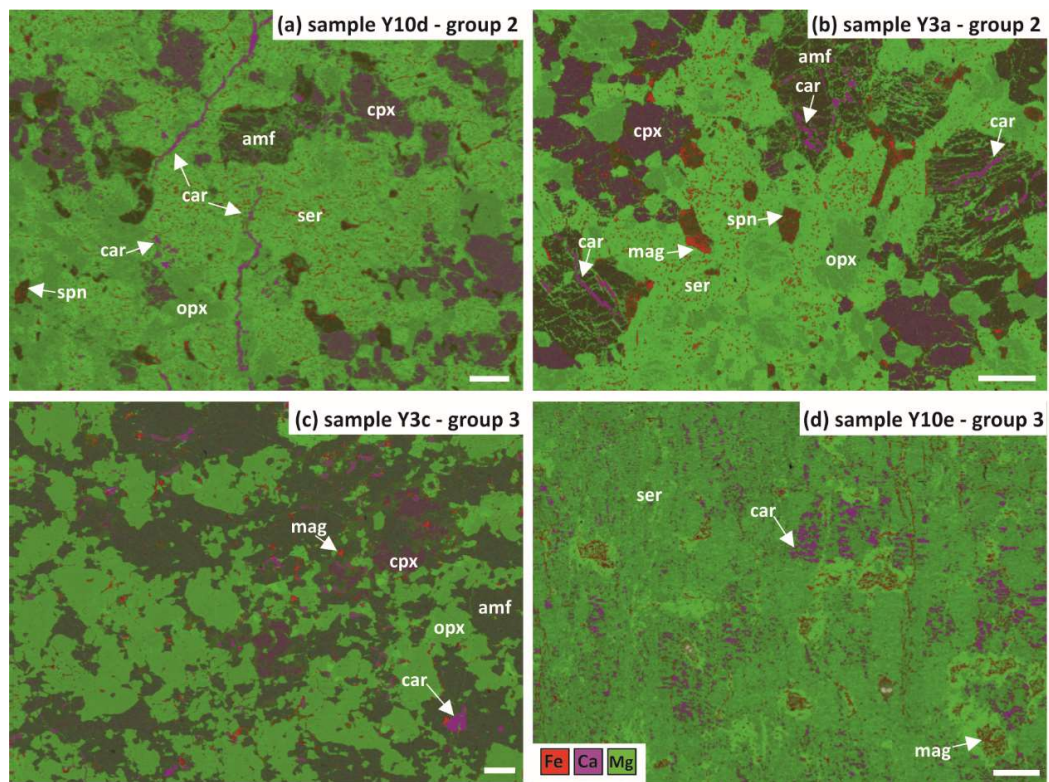
Figure 8. Element maps detailing the mineralogical and textural associations of the carbonate minerals. White scale bar = 1 mm. Abbreviations as in Figure 7.
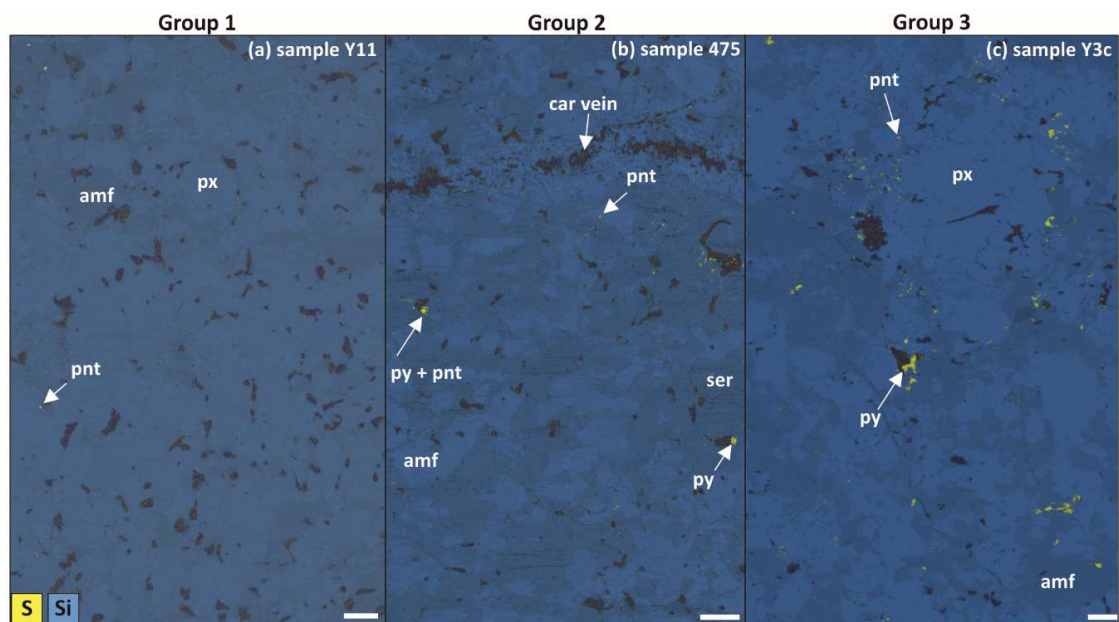
Figure 9. Element maps detailing the mineralogical and textural associations of the sulphide minerals. Note: black areas represent both oxide and carbonate mineral phases. White scale bar = 1 mm. Abbreviations: amf = amphibole; car = carbonate phase; pnt = pentlandite; px = pyroxene; py = pyrite; ser = serpentine.

6. Mineral Chemistry

6.1. Orthopyroxene

Orthopyroxenes classify as Al-rich hypersthene and exhibit the following compositional ranges: Wo = 0.2–5.0, En = 79.9–87.9; Fs = 11.9–18.8 and 1.7–4.2 wt. % Al_2O_3. On bivariate plots (Figure 10), group 1 and 2 orthopyroxenes collectively form relatively tight clusters (Figure 10), with restricted Si, Mg, Al, Ca and Fe ranges (Figure 10). Group 3 orthopyroxene compositions are broadly comparable to groups 1 and 2, although they exhibit minor Si and Mg enrichment and minor Al depletion (Figure 10).
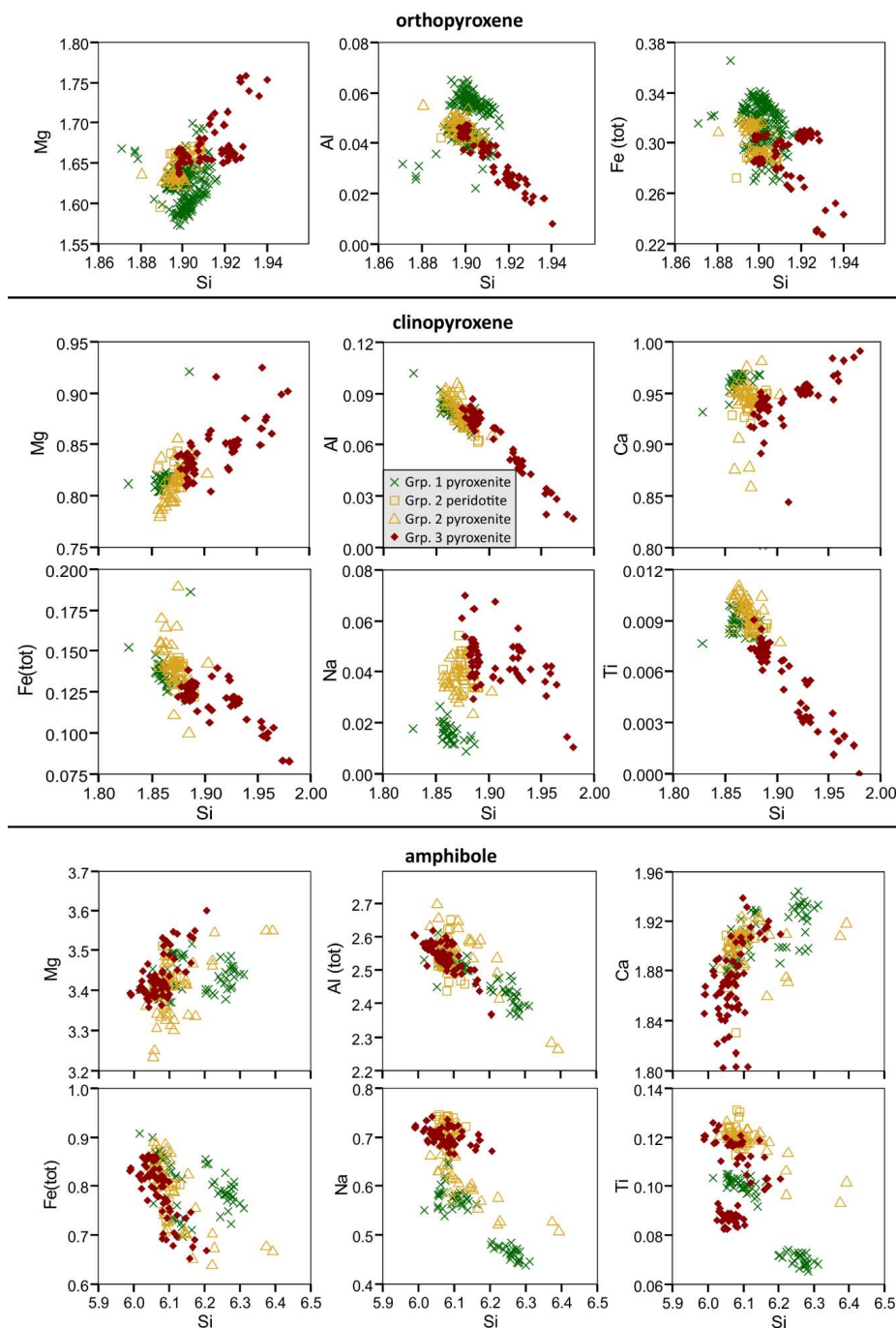
Figure 10. Bivariate plots detailing the major and minor-element compositions of orthopyroxene, clinopyroxene and amphibole. Axes are in atoms per formula unit (apfu). Amphibole analyses were originally published in Guice et al. [45].

On chondrite-normalised REE plots, group 1 orthopyroxenes exhibit concave upward patterns, negatively sloping LREE ($[La/Nd]_N$ = 0.9–5.3) and positively sloping medium (MREE) to HREE ($[Pr/Yb]_N$ = 0.04–0.17; Figure 11a).　Group 2 orthopyroxenes display similar concave upward patterns, negatively sloping LREE ($[La/Nd]_N$ = 2.7–64.0) and positively sloping MREE–HREE ($[Pr/Yb]_N$ = 0.03–1.97), although selected orthopyroxenes are slightly enriched in LREE relative to group 1 samples (Figure 11b).　Group 3 orthopyroxenes display negatively sloping LREE–MREE ($[La/Ho]_N$ = 9.7–200.0) and positively sloping HREE ($[Ho/Yb]_N$ = 0.05–0.5; Figure 11), with LREE and MREE enrichment relative to the group 1 samples (Figure 11c).
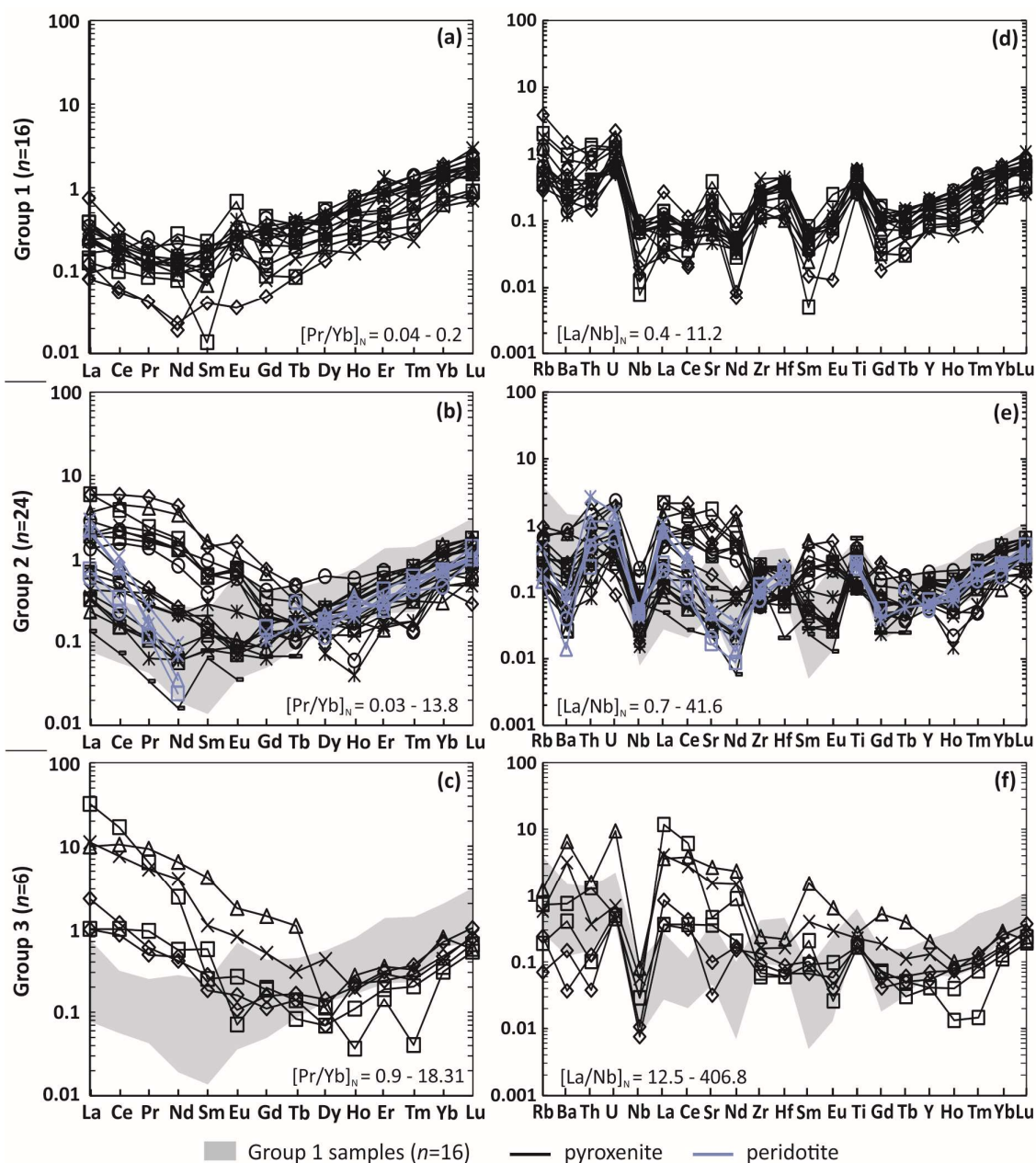
Figure 11. Chondrite-normalised REE (**a**–**c**) and primitive mantle-normalised [88] trace-element plots (**d**–**f**) for orthopyroxene grains.

On primitive mantle-normalised trace-element plots, group 1 orthopyroxenes show broadly concave upward patterns that are punctuated by positive Zr-Hf-Ti anomalies (Figure 11d). The most compatible elements exhibit positive slopes ($[Gd/Yb]_N$ = 0.1–0.3), the moderately compatible elements

are relatively flat ($[Nb/Sm]_N$ = 0.2–2.8), and there is consistent enrichment of the most incompatible elements (Rb-U; Figure 11d). The normalised trace-element patterns for group 2 orthopyroxenes also exhibit broadly concave upward patterns and positively sloping patterns for the most compatible elements ($[Gd/Yb]_N$ = 0.1–0.5; Figure 11e). However, unlike group 1, the group 2 orthopyroxenes display variable patterns for the moderately compatible elements, with some mild LREE enrichment and some mild incompatible element depletion (Rb-U; Figure 11e). Group 3 orthopyroxenes exhibit positively sloping patterns for the most compatible elements ($[Gd/Yb]_N$ = 0.2–2.3) and normalised HFSE abundances comparable to the group 1 samples (Figure 11f). However, unlike the group 1 samples, the group 3 orthopyroxenes exhibit apparent negative Nb anomalies and associated LREE enrichment (Figure 11f).

6.2. Clinopyroxene

As described in Section 5 and detailed in Figure 7, clinopyroxene is variably rimmed and replaced by amphibole on all scales. It is, therefore, possible that clinopyroxene analyses incorporate some alteration to amphibole. All clinopyroxenes classify as Al-rich diopside and exhibit the following compositional ranges (Figure 10): Wo = 41.7–51.3, En = 41.2–48.3, Fs = 4.3–10.1, and 0.9–6.4 wt. % Al_2O_3. On most major-element bivariate plots, the group 1 and 2 clinopyroxenes together form relatively tight clusters, with comparable Si, Fe, Mg, Al, Ca and Ti concentrations (Figure 10). However, group 2 clinopyroxenes are enriched in Na (0.16–0.37% Na_2O) relative to group 1 clinopyroxenes (<0.18% Na_2O; Figure 10). Group 3 clinopyroxenes show minor overlap with group 1 and 2 compositions, but exhibit significant Si and Na enrichment, significant Al and Ti depletion, minor Fe depletion, and minor Mg enrichment (Figure 10).

On chondrite-normalised REE plots, group 1 clinopyroxenes exhibit relatively flat patterns ($[Pr/Yb]_N$ = 0.3–1.9) and a relatively restricted range of normalised LREE abundances (Figure 12a). Group 2 clinopyroxenes display flat MREE–HREE patterns and normalised abundances comparable to the group 1 samples (Figure 12b). However, these clinopyroxenes display LREE enrichment ($[Pr/Yb]_N$ = 0.5–38.3) relative to the group 1 samples, with such enrichment most prominent in peridotite samples (Figure 12b). Group 3 clinopyroxenes exhibit relatively flat HREE patterns, with positively sloping LREE–MREE ($[Pr/Yb]_N$ = 6.0–219.3; Figure 12c) that are significantly enriched in LREE relative to the group 1 clinopyroxenes.

On primitive mantle-normalised trace-element plots, group 1 clinopyroxenes display flat overall patterns that are punctuated by negative Sr-Nb-Ta-Ba-Rb anomalies ($[La/Nb]_N$ = 2.0–19.9; Figure 12d). The trace-element patterns for the group 2 clinopyroxenes are comparable to the group 1 samples, but show relative LREE enrichment ($[La/Nb]_N$ = 3.2–217.1; Figure 12e). Similarly, group 3 clinopyroxenes display similar trace-element patterns to the group 1 samples, with a more pronounced enrichment in the LREE ($[La/Nb]_N$ = 28.9–873.4; Figure 12f).
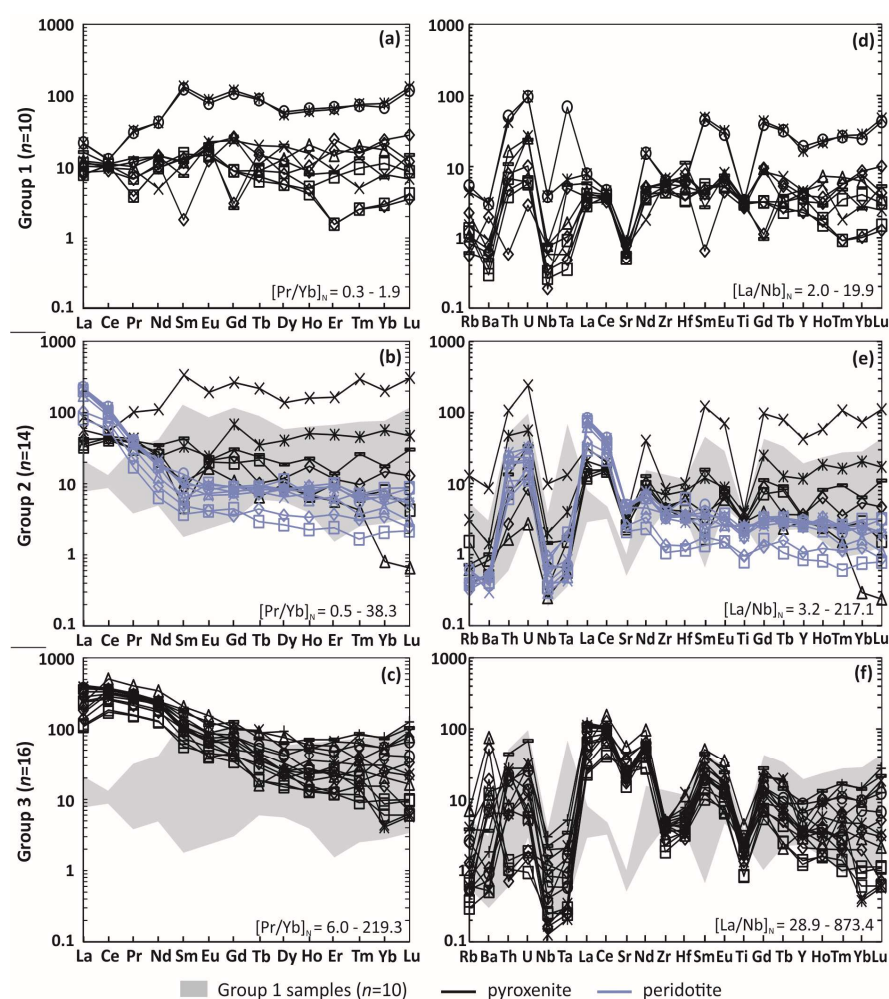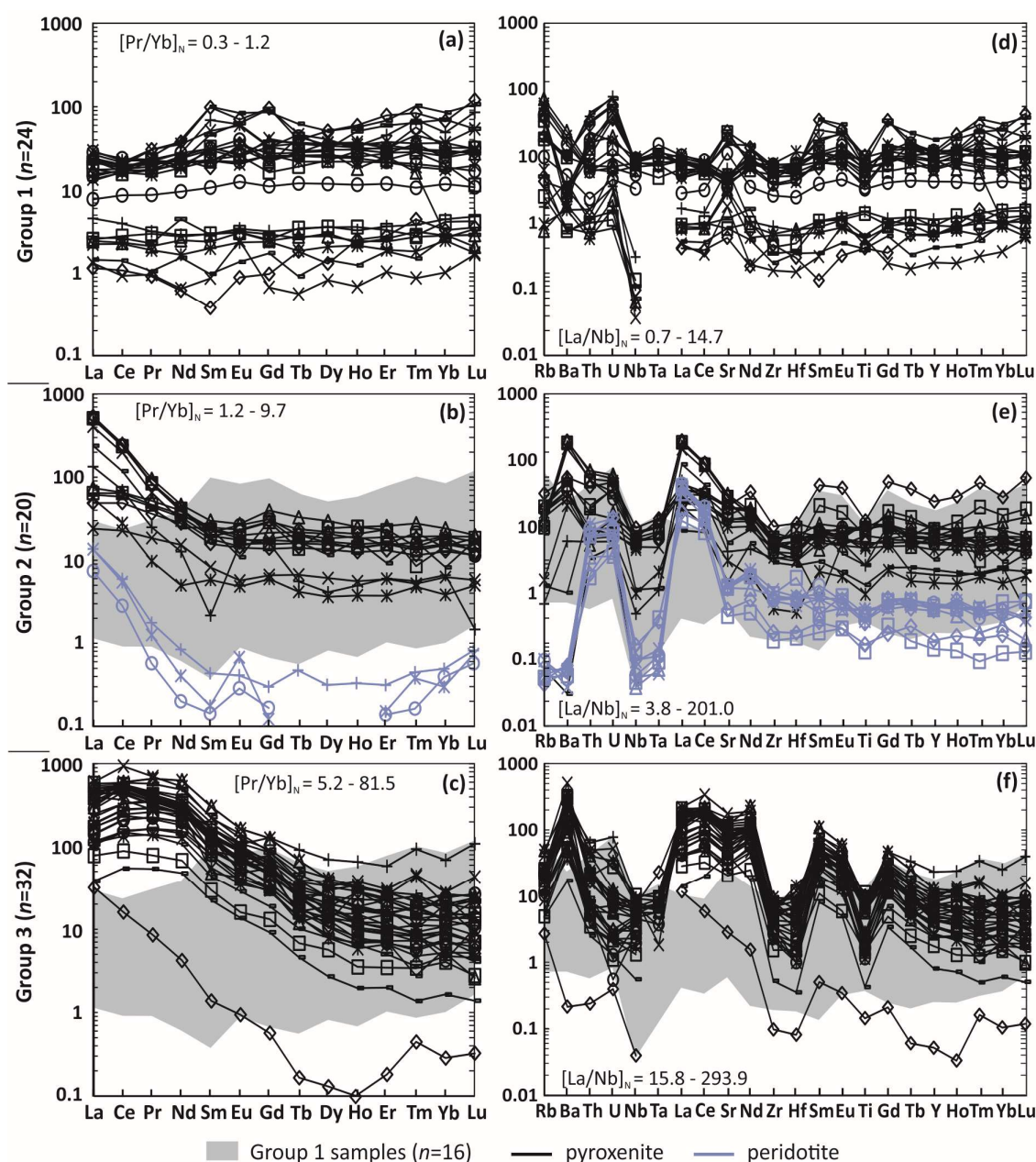
Figure 12. Chondrite-normalised REE (**a**–**c**) and primitive mantle-normalised [88] trace-element plots (**d**–**f**) for clinopyroxene grains.

6.3. Amphibole

All amphiboles classify as pargasite and exhibit the following compositional ranges (in wt. %): 41.9–45.5% SiO_2, 13.7–16.2% Al_2O_3, 1.7–2.7% Na_2O, 15.4–17.1% MgO, 11.8–13.0% CaO, 0.6–1.2% TiO_2 and 5.9–8.6% Fe_2O_3 (Figure 10; [45]). Group 1 amphiboles form two clusters on major-element bivariate plots (Figure 10), with one subgroup enriched in Si and Ca, and depleted in Na, Al and Ti relative to the other. Group 2 amphiboles are generally comparable to the Si-poor group 1 amphiboles in their Si, Mg, Al, Ca, Fe and Ti abundances, although group 2 amphiboles exhibit some Na depletion and Si enrichment relative to these group 1 amphiboles (Figure 10). Group 3 amphiboles have similar Mg, Al, Ca and Fe abundances to the Si-poor group 1 amphiboles, but are relatively enriched in Ti and Na, and relatively depleted in Ca (Figure 10).

On chondrite-normalised REE plots, group 1 amphiboles exhibit flat patterns ($[Pr/Yb]_N$ = 0.3–1.2) and a broad range of normalised REE abundances (2.1–119.2× chondrite; Figure 13a). These group 1 amphiboles can be subdivided into high total REE and low total REE subgroups that have parallel REE patterns (Figure 13a). Group 2 amphiboles display flat MREE–HREE ($[Eu/Lu]_N$ = 0.3–1.5) and negatively sloping LREE patterns ($[La/Sm]_N$ = 1.0–61.9), with peridotite samples significantly depleted in the REE relative to pyroxenite (Figure 13b). Group 3 amphiboles exhibit flat HREE, negatively sloping MREE and flat LREE ($[Pr/Yb]_N$ = 5.2–81.5), with significant LREE–MREE enrichment relative to the group 1 amphiboles (Figure 13c).

On primitive mantle-normalised trace-element plots, group 1 amphiboles generally display relatively flat patterns, with some negative Nb anomalies ([La/Nb]$_N$ = 0.7–14.7; Figure 13d). Group 2 amphiboles also exhibit flat trace-element patterns, but are punctuated by positive LREE anomalies and some negative Nb-Ta-Rb-Ba anomalies ([La/Nb]$_N$ = 3.8–201.0; Figure 13e). Group 3 amphiboles have HREE abundances comparable to the group 1 samples, but display LREE, MREE and Ba enrichment, with prominent apparent negative anomalies ([La/Nb]$_N$ = 15.8–293.9), although the Nb-Ta abundances are comparable to the group 1 samples (Figure 13f).

Figure 13. Chondrite-normalised REE (**a**–**c**) and primitive mantle-normalised [88] trace-element plots (**d**–**f**) for amphibole grains.

6.4. Carbonate Phases

As previously mentioned (Section 3.4), the fine grain size of the carbonate phases relative to the laser beam diameter sometimes resulted in the incorporation of some silicate material into the analysis.

Consequently, the succeeding descriptions should be treated as an indication of the trace-element budgets of the calcite in the Ben Strome ultramafic rocks, rather than absolute abundances.

On chondrite-normalised REE plots, carbonate analyses from group 2 samples display flat MREE–HREE patterns ([Eu/Lu]$_N$ = 0.2–1.6) and negatively sloping LREE ([La/Sm]$_N$ = 18.1–52.1; Figure 14a). On primitive mantle-normalised trace-element plots, these analyses display flat patterns for the most compatible elements (Gd-Lu), mild negative Zr-Hf anomalies and strong positive LREE anomalies ([La/Nb]$_N$ = 39.3–71.5; Figure 14b). Calcite analyses from group 3 samples display flat HREE and negatively sloping LREE–MREE ([Pr/Yb]$_N$ = 140–160.3; Figure 14c). On primitive mantle-normalised trace-element plots, these analyses exhibit flat patterns for the most compatible elements (Tb-Lu), with negative Ti-Zr-Hf anomalies, and positive MREE and LREE anomalies ([La/Nb]$_N$ = 343.8–408.8; Figure 14d).
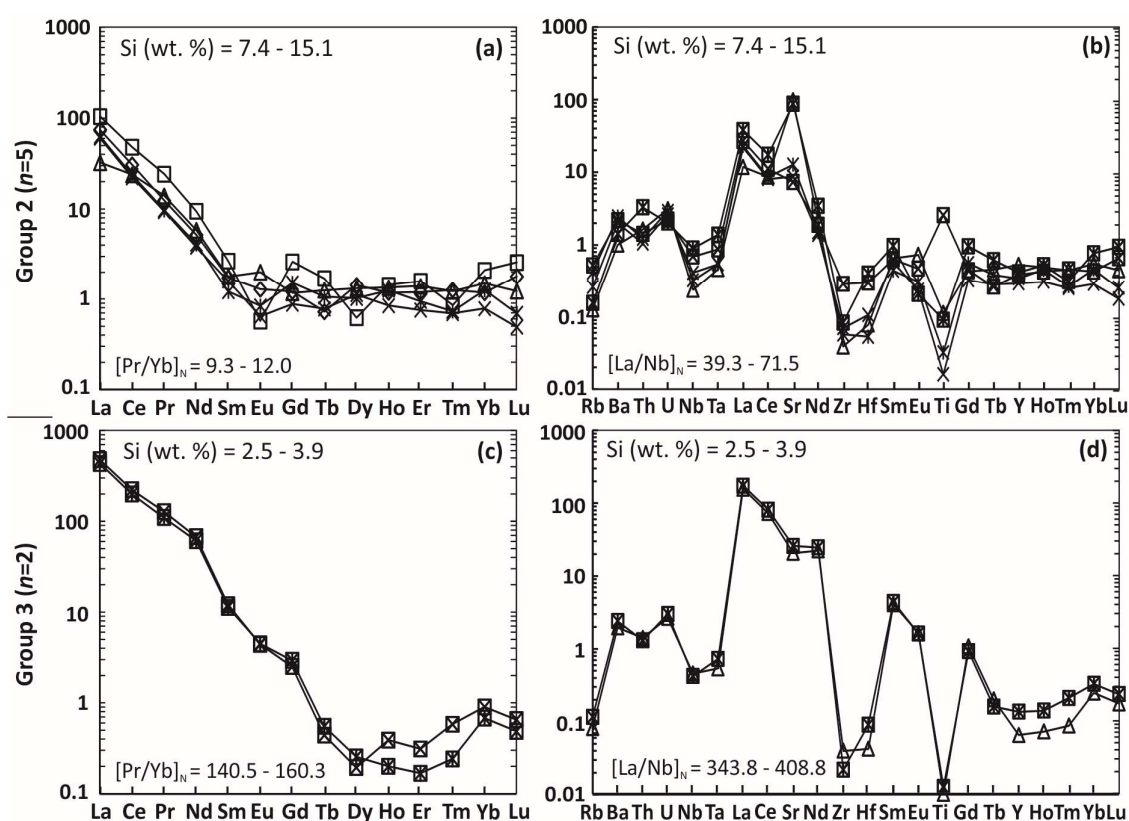
Figure 14. Chondrite-normalised REE (**a**,**c**) and primitive mantle-normalised [88] trace-element plots (**b**,**d**) for group 2 (**a**,**b**) and group 3 (**c**,**d**) carbonate grains. Note: due to the small size of carbonate grains, laser ablation (LA)-ICP-MS analyses include variable proportions of silicate material, as indicated.

7. Discussion

### 7.1. Constraining the Bulk-Rock Geochemical Controls

Despite the fact that the outlined geochemical groups may be defined by the extent (or absence) of HFSE anomalies, the absolute abundances of the HFSE are remarkably consistent between the 3 groups of ultramafic rocks in the Ben Strome Complex (Figure 4). Instead, the presence/absence of any HFSE anomalies is ultimately controlled by the degree of LREE enrichment, as demonstrated in Figure 4d,f, and it is, therefore, necessary to examine the controls of the LREE budget within the Ben Strome ultramafic rocks. The simplest hypothesis is that it could be controlled by the modal mineral abundances of individual samples, with a greater proportion of LREE-bearing mineral phases present in group 2 and 3 samples. However, the data shown in Table 1 contradict this assertion, with each geochemical group displaying a wide-range of modal mineral abundances and no systematic variation

between the groups. An alternative hypothesis is that the LREE budget of the Ben Strome ultramafic rocks could be controlled by variable trace-element compositions of specific common minerals. This is supported by the normalised REE and trace-element patterns for individual silicate minerals, with clinopyroxene (Figure 12) and, most prominently, amphibole (Figure 13) showing significant enrichment of the LREE in groups 2 and 3 relative to group 1 samples. These patterns broadly mirror those of the bulk-rock geochemistry, with strong negative HFSE anomalies only associated with group 2 and 3 samples.

Mass balance calculations, as detailed in Figure 15, were carried out to test this hypothesis. We compared measured bulk-rock trace-element patterns to those calculated using the trace-element compositions and modal mineral abundances of clinopyroxene and amphibole (Figure 15). Although the analysed calcite grains also show the LREE enrichment, we exclude them from mass balance calculations due to the extremely low modal abundance (<0.2 modal %) of these phases. We also exclude orthopyroxene from mass balance calculations, as the trace-element concentrations are 1–2 orders of magnitude lower than those of clinopyroxene and amphibole (Figures 11–13), and they therefore have a limited contribution to the trace-element budgets of the Ben Strome ultramafic rocks.

For all three modelled samples, the calculated and measured trace-element patterns are good matches (Figure 15). For sample Z11g—a group 1 sample—the measured and calculated trace-element compositions correspond well (Figure 15a), with relatively flat patterns and enrichment of the most incompatible elements (Rb-U), although the calculated pattern is slightly enriched in the most compatible elements (the HREE) relative to the measured pattern (Gd-Lu; Figure 15a). For sample Y3a—a group 2 sample—the measured and calculated trace-element compositions also correspond well (Figure 15b), displaying flat compatible element patterns (Hf-Lu), LREE enrichment, negative Nb-Ta anomalies and enrichment of the most incompatible elements (Ba-U), although the calculated composition is slightly depleted in Nb, Ta, Ba, Th and U (Figure 15b). For sample Y3d—a group 3 sample—the measured and calculated trace-element patterns (Figure 15c) show LREE and MREE enrichment and associated negative Nb-Ta-Zr-Hf-Ti anomalies. Although the measured and calculated patterns are consistently parallel, the latter is enriched relative to the former (Figure 15c), suggesting that the measured trace-element compositions for clinopyroxene and amphibole in this sample are not wholly representative.

The consistent correspondence between the calculated and measured trace-element patterns indicates that the unique trace-element compositions of the group 2 and 3 samples cannot be attributed to crystallisation of LREE-bearing mineral phases during fractionation. Rather, these data are in general agreement with a hypothesis whereby the trace-element budgets of the Ben Strome ultramafic rocks are controlled by the composition of clinopyroxene and amphibole. In group 2 and 3 samples, the LREE contents in clinopyroxene and amphibole are 1–2 orders of magnitude greater than in the group 1 samples, with this LREE enrichment responsible for the presence of apparent HFSE anomalies in the bulk-rock data. The succeeding section therefore focuses on identifying the source of this LREE enrichment in the context of several hypotheses relating to the origin of HFSE anomalies.
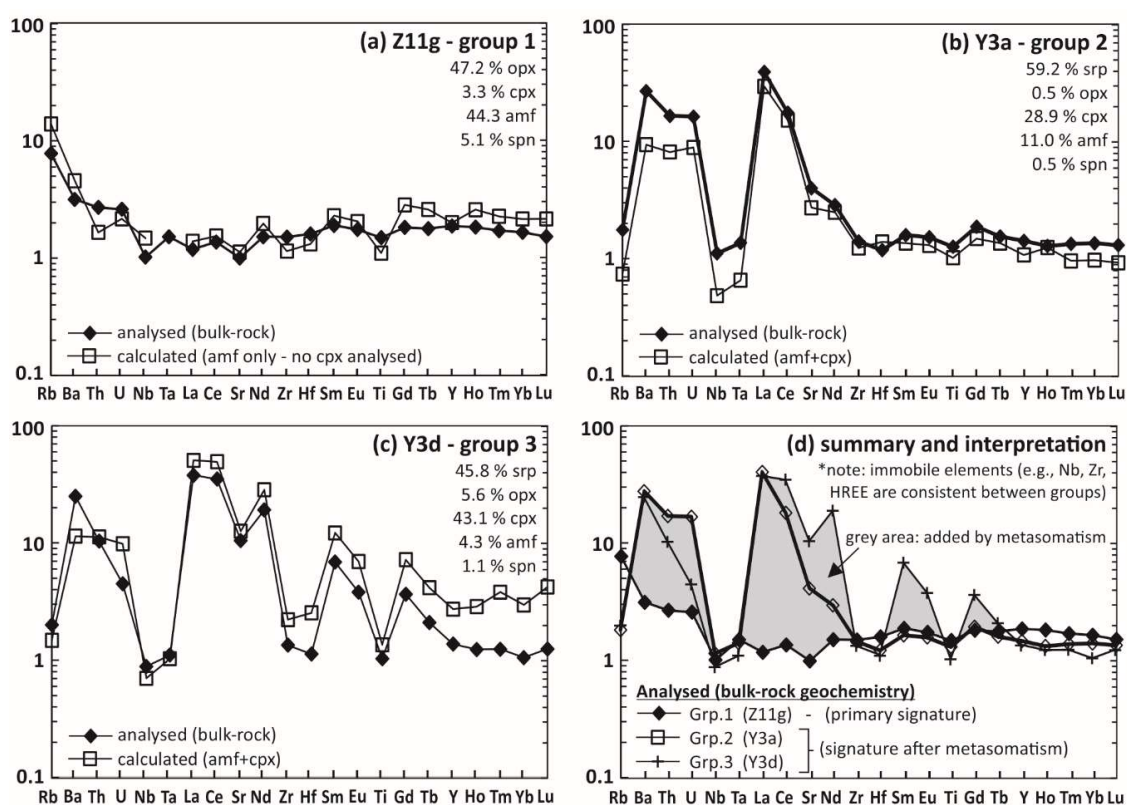
Figure 15. (**a**–**c**) Primitive mantle-normalised [88] trace-element plots displaying the mass balance calculations for the Ben Strome ultramafic rocks; (**d**) Primitive mantle-normalised trace-element plot detailing an interpretation of the 3 patterns displayed in parts (**a**–**c**).

7.2. Origin of the High Field Strength Elements Anomalies

7.2.1. Primary Magmatic Processes

As outlined in above, several authors have used HFSE anomalies present in intrusive and/or extrusive Archaean ultramafic-mafic suites as evidence that these rocks (interpreted as cumulates [45]) were produced by subduction-related magmatism [20,26,27]. Considering the bulk-rock geochemical data alone, a similar interpretation could be offered for the Ben Strome ultramafic rocks. However, such an interpretation—whereby the LREE enrichment of clinopyroxene and amphibole, and associated bulk-rock HFSE anomalies shown by the group 2 and 3 ultramafic rocks result from fractional crystallisation of an initial magma inherently depleted in the HFSE—is contradicted by the evidence presented in this study. First, the group 2 and 3 ultramafic rocks do not represent the most fractionated portions of the layered complex, with bulk-rock MgO values for these samples (18–43 wt. % MgO) showing significant overlap with the group 1 samples (27–48 wt. % MgO). The bulk-rock data are supported by the composition of clinopyroxene, which shows no correlation between MgO and La ($R^2 = 0.01$), indicating that the LREE-rich composition of this mineral phase in the group 2 and 3 samples cannot be attributed to fractional crystallisation. Second, group 2 and 3 samples exhibit a poor correlation between Yb and the LREE ($R^2 = 0.01$–0.06; Figure 6), suggesting that secondary processes have mobilised the LREE. This interpretation is supported by the moderate to strong correlation ($R^2 = 0.5$–0.7) between Ba (a fluid mobile element) and the LREE, and by the strong correlation ($R^2 \geq 0.9$) between Sr (another fluid mobile element) and the LREE. In contrast, the group 1 samples display a good correlation between Yb and the LREE ($R^2 = 0.5$–0.8; Figure 6), implying that these rocks have not experienced the same mobility of these elements. Third, samples of different geochemical groups are often located less than a metre (stratigraphically) from one another, as detailed in Figure 3. As a consequence, if the variable LREE contents of clinopyroxene and amphibole were to be achieved

only by magmatic processes and thus using a common magma, it could only be accomplished through extreme (and implausible) variations in partition coefficients on a metre-scale. Thus, primary magmatic processes such as fractional crystallisation cannot explain the variation in composition between the geochemical groups.

7.2.2. Crustal Contamination

Alternatively, several authors have attributed negative HFSE anomalies to crustal contamination [5,89], with this process potentially occurring during the emplacement of the Ben Strome Complex into the surrounding TTG gneiss [45]. This hypothesis was tested by performing simple mixing calculations to model the observed groups 2 and 3 compositions, as presented in Figure 16. Calculations involved mixing a group 1 sample (Z11g; Table 2) with the average composition of TTG gneiss analysed for the Central Region LGC [90]. The calculated (chondrite-normalised) REE patterns indicate that some of the group 2 ultramafic rocks can be roughly re-created by mixing the group 1 ultramafic sample with 10–40% TTG gneiss (Figure 16). However, this modelling predicts SiO_2 contents of between 44 and 51 wt. %, which does not correlate with the 40 to 48 wt. % measured in the group 2 ultramafic samples. Moreover, the chondrite-normalised REE patterns displayed by the group 3 ultramafic rocks could not be re-created by any mixing scenario (Figure 16). Consequently, the modelling presented in Figure 16 suggests that simple mixing between group 1 ultramafic rocks and local TTG gneiss offers a limited and inherently poor solution for the source of the LREE enrichment and HFSE anomalies displayed by the group 2 and 3 ultramafic rocks.

The crustal contamination hypothesis is also questioned by other evidence presented in this study. First, LREE enrichment and HFSE anomalies generated by crustal contamination are commonly associated with SiO_2 enrichment [5], but bulk-rock SiO_2 and La are poorly correlated ($R^2 = 0.02$) in the Ben Strome ultramafic rocks. Second, the groups 2 and 3 samples are randomly distributed throughout the Ben Strome Complex, rather than being preferentially concentrated towards the edges, where interactions with the surrounding TTG might be expected to be most intense. Moreover, group 2 samples may be located less than 30 cm (stratigraphically) from group 1 samples located both above and below, as shown in Figure 3d. Although this hypothesis cannot be completely ruled out without having conducted Hf and/or Nd isotopes on bulk-rock samples, the evidence presented here indicates that crustal contamination is unlikely the source of the HFSE anomalies in the Ben Strome ultramafic rocks.
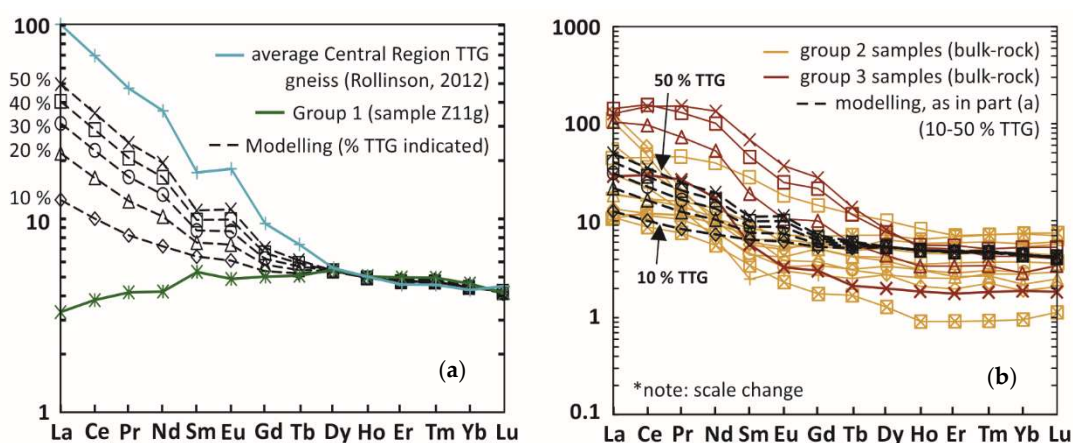
Figure 16. Chondrite-normalised [88] REE plots detailing the mixing calculations used to test the crustal contamination hypothesis. (**a**) modelling; (**b**) modelling and bulk-rock analyses of samples with high field strength-elements (HFSE) anomalies.

7.2.3. Secondary Metasomatism

As outlined in Section 7.2.1, it is unlikely that the geochemical signatures displayed by the groups 2 and 3 ultramafic rocks reflect primary magmatic processes involving a single magma. Rather, subsequent element mobility is likely responsible for the LREE enrichment and associated HFSE anomalies displayed by the bulk-rock geochemistry for these samples (Figures 6 and 15d). In contrast, the group 1 samples do not appear to have experienced the same LREE mobility, with the trace-element compositions displayed by these samples interpreted to most closely resemble primary signatures (Figure 15d). As stated above, this interpretation is supported by the moderate to strong positive correlation between Yb and the LREE (R^2 = 0.5–0.9) in the group 1 samples, and the absence of any correlation between these elements in the groups 2 and 3 samples (Figure 6). Moreover, the absolute abundances of elements considered to be immobile in the Ben Strome Complex (e.g., Nb, Ta, Zr, Hf, Ti, Y and the HREE) are comparable between all 3 geochemical groups (Figure 4), demonstrating that the trace-element budgets of the Ben Strome ultramafic rocks were likely comparable prior to metasomatism. This interpretation supports the mineral chemistry study of Rollinson and Gravestock [81], who attributed similar LREE enrichment of clinopyroxene in layered ultramafic rocks from Camas nam Buth (located near Scourie, 13 km NW of Ben Strome; Figure 2) to secondary, rather than primary, processes.

Although the relatively LREE-rich TTG gneiss that surrounds the Ben Strome Complex represents a potential local source of LREE, there is a limited number of processes capable of mobilising, transporting and depositing these elements [91]. One possibility, as initially proposed by Rollinson and Gravestock [81], is that the groups 2 and 3 Ben Strome ultramafic rocks interacted with LREE-rich, felsic melts produced during localised partial melting, which occurred during the 2.7 Ga Badcallian metamorphic event. This hypothesis is supported by the evidence for partial melting at Ben Strome [45] and wider LGC [46,47]. However, it is questioned by the absence of any petrographic evidence for such melts at the macro or micro scale within the group 2 or 3 rocks. Moreover, there is no recorded field evidence for felsic partial melts cross-cutting ultramafic rocks, either at Ben Strome [45] or elsewhere in the LGC [46,47,76]. This hypothesis is also hard to reconcile with the composition of felsic partial melts reported by Johnson et al. [46], as all group 3 and some group 2 ultramafic rocks contain higher concentrations of LREE than these melts.

Alternatively, mobilisation, transport and deposition of the LREE (in the groups 2 and 3 ultramafic rocks) may have been facilitated by a CO_2-rich, H_2O-rich fluid associated with amphibolitisation. This is further to the work of Beach and Tarney [92], who proposed that hydrothermal fluids were responsible for significant element mobility during the retrogression of the granulite-facies mineral assemblages in the LGC. The CO_2-rich, H_2O-rich fluid hypothesis is directly supported by the near-exclusive presence of LREE-rich carbonate mineral phases (mixed analyses contain <122 ppm La; Figure 14) within the groups 2 and 3 samples (Figure 8), which may represent the relics of fluid-rock interaction. This hypothesis is also consistent with the more intense amphibolitisation of clinopyroxene in the groups 2 and 3 samples relative to the group 1 samples (Figure 7), and with the composition of amphibole and clinopyroxene, which reflect and ultimately control the bulk-rock trace-element patterns (Figures 12, 13 and 15). Moreover, the groups 2 and 3 samples show evidence for introduction of S via hydrothermal fluids (as pyrite; Figure 9) that is absent in the group 1 samples.

Amphibolitisation of the Ben Strome ultramafic rocks was probably polyphase (Figure 7), occurring during both the Inverian and Laxfordian metamorphic events at ca. 2.48 and 1.9–1.6 Ga respectively [60–62]. Based on the cross-cutting carbonate veins present in group 2 and 3 ultramafic rocks, we here suggest that the CO_2-rich, H_2O-rich fluids responsible for these rocks in the LREE were associated with the later stage, 1.9–1.6 Ga Laxfordian metamorphic event, when the rocks had already been amphibolitised. This interpretation is supported by the presence of the large, E–W-trending Laxfordian shear zone that cross-cuts the Ben Strome Complex, which plausibly provided a conduit for fluids that subsequently exploited a discrete fracture network in the Ben Strome Complex. Although CO_2 and H_2O-rich fluids are generally not considered the most efficient

mechanism for transporting and concentrating the LREE [91], several authors report LREE mobility associated with CO_2-rich fluids, particularly in the upper mantle [7,10,13,91,93,94]. In these examples, the composition of clinopyroxene and amphibole often exhibit elevated Na and Si, and depleted Al and Ti concentrations relative to un-metasomatised samples, with these chemical effects reflected by the group 2 and 3 Ben Strome ultramafic rocks (Figure 10; [13,93,94]).

Based on these combined characteristics, the HFSE anomalies displayed by the groups 2 and 3 samples are most consistent with processes involving interaction with a CO_2 and H_2O-rich hydrothermal fluid associated with amphibolitisation and the Laxfordian metamorphic event, which represents the second phase of amphibolite-facies metamorphism experienced by the LGC. Therefore, only the trace-element patterns displayed by the group 1 samples represent the original composition of the Ben Strome ultramafic rocks immediately after they crystallised (Figures 4b and 15d).

7.3. Implications for Geochemical Fingerprinting in Archaean Cratons

Although the role of modern-style plate tectonic processes (including Phanerozoic-style subduction) remains highly controversial, HFSE anomalies in extrusive/intrusive ultramafic-mafic Archaean assemblages have been widely cited as evidence for Archaean subduction-related magmatism (Figure 1; [20–27]). Such interpretations assume that, as with Phanerozoic subduction-related magmatism, the HFSE anomalies are generated by the enrichment of subduction-mobile elements (e.g., the alkali metals and LREE) relative to subduction-immobile elements (e.g., the HFSE; [4,6]). However, the data presented in this study indicate that apparent negative HFSE anomalies can also be generated by discrete secondary processes that produce enrichment of LREE while the HFSE remain at (or close to) primary concentrations. This is further to previous research suggesting that the HFSE anomaly can also be generated by crustal contamination [5] and interaction with the SCLM [6]. We therefore consider the HFSE anomaly to represent an unreliable proxy for Archaean subduction that should be treated with extreme caution, particularly in Archaean terranes such as the North Atlantic Craton that have experienced high-grade and polyphase metamorphism.

Some studies that invoke a subduction-related origin for HFSE anomalies in other Archaean intrusive/extrusive ultramafic-mafic assemblages offer several (and inconsistent) lines of evidence and argument to demonstrate that the rocks have not been subject to element mobility [20,21,26,27], with LOI values lower than 3.5 wt. % and the assumed immobility of the REE during hydrothermal alteration most commonly cited. The assertion that low LOI values can be used to 'screen' altered samples is straightforwardly contradicted by the data presented here, with the group 1 samples, which are here interpreted to have experienced limited element mobility, displaying values of up to 9 wt. %. The groups 2 and 3 samples, which have experienced significant mobility of the LREE, exhibit LOI values of up to 8 wt. %, but some of these samples display values of less than 1 wt. % meaning they would appear 'fresh' under as simple LOI screening process. If we had screened the Ben Strome ultramafic samples based on this 3.5 wt. % LOI rule, we would have discarded 10 (out of 20) group 1 samples, 7 (out of 11) group 2 samples and 2 (out of 4) group 3 samples. This supports the work of Babechuk and Kamber [95], who observed low (<5% wt. %) LOI values in samples that had demonstrably experienced significant mobility of fluid mobile elements. With respect to the assumed immobility of the REE during hydrothermal alteration, this paper is the latest of a plethora of studies demonstrating that the REE can be mobilised by hydrothermal alteration of varying styles [7,10,13,91,93]. It is, therefore, clear that such assumptions are frequently misplaced, particularly in high-grade cratonic regions that have experienced polyphase and high-grade metamorphism.

The findings presented here question some previous interpretations of Archaean ultramafic-mafic assemblages as associated with subduction-related magmatism, particularly where bulk-rock HFSE anomalies are cited as primary evidence. It is possible that the HFSE anomalies displayed by these examples may have been generated by discrete secondary processes akin to those described here, with the role of subduction during the Archaean potentially overestimated as a result. While it is entirely possible that subduction-related magmatism contributed to crustal growth during the

Archaean, this finding must rest on reliable evidence. It is clear from the evidence presented here that a comprehensive assessment of element mobility and petrography (using well characterised and spatially constrained samples) is a minimum requirement prior to attaching a geodynamic interpretation, further demonstrating that geochemical fingering should be assessed on a location-specific basis [2,95–97]. Given the effects of high-grade metamorphism and associated processes, which are unique on the terrane-scale, individual occurrences of ultramafic-mafic units should be placed within the regional framework to constrain primary geochemical signatures, with a 'one-size fits all' approach to bulk-rock trace-element geochemical data inappropriate in such complex regions.

8. Conclusions

1. Negative HFSE anomalies, which are commonly used as evidence for subduction-related magmatism in the Archaean, can also be generated by secondary processes that may be petrographically discrete. In the case of the Ben Strome Complex, these anomalies were most likely generated by LREE enrichment during metasomatism by a CO_2 and H_2O-rich hydrothermal fluid associated with amphibolitisation, rather than reflecting a signature inherited from a subduction-related magma.

2. Our data demonstrate that the HFSE anomaly should be used (as a proxy for Archaean subduction) with extreme caution, particularly in Archaean terranes that have experienced multiple phases of high-grade metamorphism and where the rocks are likely to have experienced differential element mobilities. Consequently, conducting a comprehensive assessment of element mobility and petrography (using well characterised and spatially constrained samples) is a minimum requirement prior to assigning any geodynamic interpretation to Archaean ultramafic-mafic units. In cases where such assessments have not been undertaken, it is possible that subduction-related interpretations have been erroneously invoked, with the role of subduction as an Archaean geodynamic process potentially overestimated as a result.

References

1. Pearce, J.A.; Cann, J.R. Tectonic setting of basic volcanic rocks determined using trace element analyses. *Earth Planet. Sci. Lett.* **1973**, *19*, 290–300. [CrossRef]
2. Condie, K.C. TTGs and adakites: Are they both slab melts? *Lithos* **2005**, *80*, 33–44. [CrossRef]

3. Pearce, J.A. Geochemical fingerprinting of oceanic basalts with applications to ophiolite classification and the search for Archean oceanic crust. *Lithos* **2008**, *100*, 14–48. [CrossRef]

4. Klemme, S.; Prowatke, S.; Hametner, K.; Gunther, D. Partitioning of trace elements between rutile and silicate melts: Implications for subduction zones. *Geochim. Cosmochim. Acta* **2005**, *69*, 2361–2371. [CrossRef]

5. Arndt, N. Why was flood volcanism on submerged continental platforms so common in the Precambrian? *Precambrian Res.* **1999**, *97*, 155–164. [CrossRef]

6. Pearce, J.A. Geochemical Fingerprinting of the Earth's Oldest Rocks. *Geology* **2014**, *42*, 175–176. [CrossRef]

7. Wood, S.A. The aqueous geochemistry of the rare-earth elements and yttrium. *Chem. Geol.* **1990**, *82*, 159–186. [CrossRef]

8. Lee, J.H.; Byrne, R.H. Complexation of trivalent rare earth elements (Ce, Eu, Gd, Tb, Yb) by carbonate ions. *Geochemica Cosmochim. Acta* **1993**, *57*, 295–302.

9. Rudnick, R.L.; Mcdonough, W.F.; Chappell, B.W. Carbonatite metasomatism in the northern Tanzanian mantle: petrographic and geochemical characteristics. *Earth Planet. Sci. Lett.* **1993**, *114*, 463–475. [CrossRef]

10. Lahaye, Y.; Arndt, N.; Byerly, G.; Chauvel, C.; Fourcade, S.; Gruau, G. The influence of alteration on the trace-element and Nd isotopic compositions of komatiites. *Chem. Geol.* **1995**, *126*, 43–64. [CrossRef]

11. Smith, M.P.; Henderson, P.; Campbell, L.S. Fractionation of the REE during hydrothermal processes: Constraints from the Bayan Obo Fe-REE-Nb deposit, Inner Mongolia, China. *Geochim. Cosmochim. Acta* **2000**, *64*, 3141–3160. [CrossRef]

12. Rolland, Y.; Cox, S.; Boullier, A.; Pennacchioni, G.; Mancktelow, N. Rare earth and trace element mobility in mid-crustal shear zones: Insights from the Mont Blanc Massif (Western Alps). *Earth Planet. Sci. Lett.* **2003**, *214*, 203–219. [CrossRef]

13. Powell, W.; Zhang, M.; Reilly, S.Y.O.; Tiepolo, M. Mantle amphibole trace-element and isotopic signatures trace multiple metasomatic episodes in lithospheric mantle, western Victoria, Australia. *Lithos* **2004**, *75*, 141–171. [CrossRef]

14. Metrich, N.; Bertagnini, A.; Landi, P.; Rosi, M. Crystallization Driven by Decompression and Water Loss at Stromboli Volcano (Aeolian Islands, Italy). *J. Petrol.* **2001**, *42*, 1471–1490. [CrossRef]

15. Metrich, N.; Bertagnini, A.; Landi, P.; Rosi, M.; Belhadj, O. Triggering mechanism at the origin of paroxysms at Stromboli (Aeolian Archipelago, Italy): The 5 April 2003 eruption. *Geophys. Res. Lett.* **2005**, *32*, 3–6. [CrossRef]

16. Landi, P.; Francalanci, L.; Pompilio, M.; Rosi, M.; Corsaro, R.A. The December 2002–July 2003 effusive event at Stromboli volcano, Italy: Insights into the shallow plumbing system by petrochemical studies. *J. Volcanol. Geotherm. Res.* **2006**, *155*, 263–284. [CrossRef]

17. Corazzato, C.; Francalanci, L.; Menna, M.; Petrone, C.M.; Renzulli, A. What controls sheet intrusion in volcanoes? Structure and petrology of the Stromboli sheet complex, Italy. *J. Volcanol. Geotherm. Res.* **2008**, *173*, 26–54. [CrossRef]

18. Renzulli, A.; Del Moro, S.; Menna, M.; Landi, P.; Piermattei, M. Transient processes in Stromboli's shallow basaltic system inferred from dolerite and magmatic breccia blocks erupted during the 5 April 2003 paroxysm. *Bull. Volcanol.* **2009**, *71*, 795–813. [CrossRef]

19. Vezzoli, L.; Renzulli, A.; Menna, M. Growth after collapse: The volcanic and magmatic history of the Neostromboli lava cone (island of Stromboli, Italy). *Bull. Volcanol.* **2014**, *76*, 24. [CrossRef]

20. Manya, S. Geochemistry and petrogenesis of volcanic rocks of the Neoarchaean Sukumaland Greenstone Belt, northwestern Tanzania. *J. Afr. Earth Sci.* **2004**, *40*, 269–279. [CrossRef]

21. Ordóñez-Calderón, J.C.; Polat, A.; Fryer, B.J.; Appel, P.W.U.; Van Gool, J.A.M.; Dilek, Y.; Gagnon, J.E. Geochemistry and geodynamic origin of the Mesoarchean Ujarassuit and Ivisaartoq greenstone belts, SW Greenland. *Lithos* **2009**, *113*, 133–157. [CrossRef]

22. Manikyamba, C.; Kerrich, R. Geochemistry of alkaline basalts and associated high-Mg basalts from the 2.7 Ga Penakacherla Terrane, Dharwar craton, India: An Archean depleted mantle-OIB array. *Precambrian Res.* **2011**, *188*, 104–122. [CrossRef]

23. Yellappa, T.; Santosh, M.; Chetty, T.R.K.; Kwon, S.; Park, C.; Nagesh, P.; Mohanty, D.P.; Venkatasivappa, V. A Neoarchean dismembered ophiolite complex from southern India: Geochemical and geochronological constraints on its suprasubduction origin. *Gondwana Res.* **2012**, *21*, 246–265. [CrossRef]

24. Yellappa, T.; Venkatasivappa, V.; Koizumi, T.; Chetty, T.R.K.; Santosh, M.; Tsunogae, T. Journal of Asian Earth Sciences The mafic-ultramafic complex of Aniyapuram, Cauvery Suture Zone, southern India: Petrological and geochemical constraints for Neoarchean suprasubduction zone tectonics. *J. Asian Earth Sci.* **2014**, *95*, 81–98. [CrossRef]

25. Szilas, K.; Van Hinsberg, V.J.; Kisters, A.F.M.; Hoffmann, J.E.; Windley, B.F.; Kokfelt, T.F.; Scherstén, A.; Frei, R.; Rosing, M.T.; Münker, C. Remnants of arc-related Mesoarchaean oceanic crust in the Tartoq Group of SW Greenland. *Gondwana Res.* **2013**, *23*, 436–451. [CrossRef]

26. Wang, D.; Guo, J.; Huang, G.; Scheltens, M. The Neoarchean ultramafic-mafic complex in the Yinshan Block, North China Craton: Magmatic monitor of development of Archean lithospheric mantle. *Precambrian Res.* **2015**, *270*, 80–99. [CrossRef]

27. Guo, R.; Liu, S.; Bai, X.; Wang, W. A Neoarchean subduction recorded by the Eastern Hebei Precambrian basement, North China Craton: Geochemical fingerprints from metavolcanic rocks of the Saheqiao-Shangying-Qinglong supracrustal belt. *J. Asian Earth Sci.* **2017**, *135*, 347–369. [CrossRef]

28. Stern, R.J. Evidence from ophiolites, blueschists, and ultrahigh-pressure metamorphic terranes that the modern episode of subduction tectonics began in Neoproterozoic. *Geology* **2005**, *33*, 557–560. [CrossRef]

29. Stern, R.J. Modern-style plate tectonics began in Neoproterozoic time: An alternative interpretation of Earth's tectonic history. *Spec. Publ. Geol. Soc. Am.* **2008**, *440*, 265–280.

30. Kearey, P.; Klepeis, K.A.; Vine, F.J. *Global Tectonics*, 3rd ed.; Wiley-Blackwell: Hoboken, NJ, USA, 2009.

31. Arndt, N.T. Formation and Evolution of the Continental Crust. *Geochem. Perspect.* **2013**, *2*, 405–533. [CrossRef]

32. Bédard, J.H.; Harris, L.B.; Thurston, P.C. The hunting of the snArc. *Precambrian Res.* **2013**, *229*, 20–48. [CrossRef]

33. Kamber, B.S. The evolving nature of terrestrial crust from the Hadean, through the Archaean, into the Proterozoic. *Precambrian Res.* **2015**, *258*, 48–82. [CrossRef]

34. De Wit, M.J.; De Ronde, C.E.J.; Tredoux, M.; Roering, C.; Hart, R.J.; Armstrong, R.A.; Green, R.W.E.; Peberdy, E.; Hart, R.A. Formation of an Archaean continent. *Nature* **1992**, *357*, 553–562. [CrossRef]

35. Friend, C.R.L.; Nutman, A.P.; The, A.; Isua, E. Eoarchean ophiolites? New evidence for the debate on the Isua supracrustal belt, southern west Greenland. *Am. J. Sci.* **2010**, *310*, 826–861. [CrossRef]

36. Furnes, H.; Dilek, Y.; de Wit, M. Precambrian greenstone sequences represent different ophiolite types. *Gondwana Res.* **2015**, *27*, 649–685. [CrossRef]

37. Hastie, A.R.; Fitton, J.G.; Bromiley, G.D.; Butler, I.B.; Odling, N.W.A. The origin of Earth's first continents and the onset of plate tectonics. *Geology* **2016**, 855–858. [CrossRef]

38. Polat, A.; Kokfelt, T.; Burke, K.C.; Kusky, T.M.; Bradley, D.C.; Dziggel, A.; Kolb, J.; William, P.; Polat, A.; Kokfelt, T.; et al. Lithological, structural, and geochemical characteristics of Mesoarchean Târtoq greenstone belt, southern West Greenland, and the Chugach-Prince William accretionary complex, southern Alaska: evidence for uniformitarian plate-tectonic processes. *Can. J. Earth Sci.* **2016**, *53*, 1336–1371. [CrossRef]

39. Johnson, T.E.; Brown, M.; Gardiner, N.J.; Kirkland, C.L.; Smithies, R.H. Earth's first stable continents did not form by subduction. *Nature* **2017**, *543*, 239–242. [CrossRef] [PubMed]

40. Bédard, J.H. Stagnant lids and mantle overturns: Implications for Archaean tectonics, magmagenesis, crustal growth, mantle evolution, and the start of plate tectonics. *Geosci. Front.* **2018**, *9*, 19–49. [CrossRef]

41. Van Kranendonk, M.J.; Collins, W.J.; Hickman, A.; Pawley, M.J. Critical tests of vertical vs. horizontal tectonic models for the Archaean East Pilbara Granite-Greenstone Terrane, Pilbara Craton, Western Australia. *Precambrian Res.* **2004**, *131*, 173–211. [CrossRef]

42. Dhuime, B.; Wuestefeld, A.; Hawkesworth, C.J. Emergence of modern continental crust about 3 billion years ago. *Nat. Geosci.* **2015**, *8*, 552–555. [CrossRef]

43. Hopkins, M.; Harrison, T.M.; Manning, C.E. Low heat flow inferred from >4 Gyr zircons suggests Hadean plate boundary interactions. *Nature* **2008**, *456*, 493–496. [CrossRef] [PubMed]

44. Hamilton, W.B. Plate tectonics began in Neoproterozoic time, and plumes from deep mantle have never operated. *Lithos* **2011**, *123*, 1–20. [CrossRef]

45. Guice, G.L.; McDonald, I.; Hughes, H.S.R.; MacDonald, J.M.; Blenkinsop, T.G.; Goodenough, K.M.; Faithfull, J.W.; Gooday, R.J. Re-evaluating ambiguous age relationships in Archean cratons: Implications for the origin of ultramafic-mafic complexes in the Lewisian Gneiss Complex. *Precambrian Res.* **2018**, *311*, 136–156. [CrossRef]

46. Johnson, T.E.; Fischer, S.; White, R.W.; Brown, M.; Rollinson, H.R. Archaean intracrustal differentiation from partial melting of metagabbro-field and geochemical evidence from the central region of the Lewisian complex, NW Scotland. *J. Petrol.* **2012**, *53*, 2115–2138. [CrossRef]

47. Johnson, T.E.; Fischer, S.; White, R.W. Field and petrographic evidence for partial melting of TTG gneisses from the central region of the mainland Lewisian complex, NW Scotland. *J. Geol. Soc. Lond.* **2013**, *170*, 319–326. [CrossRef]

48. Park, R.G.; Stewart, A.D.; Wright, A.E. The Hebridean Terrane. In *The Geology of Scotland*; Trewin, N.H., Ed.; Geological Society of London: London, UK, 2002.

49. Peach, B.N.; Horne, J.; Gunn, A.G.; Clough, C.T.; Geikie, A.; Hinxman, L.W.; Teall, J.J.H. The Geological Structure of the North-West Highlands. In *Memoir of the Geological Survey of Great Britain*; HMSO: Edimburgh, UK, 1907.

50. Sutton, J.; Watson, J.V. The pre-Torridonian metamorphic history of the Loch Torridon and Scourie areas in the northwest Highland, and its bearing on the chronological classification of the Lewisian. *Q. J. Geol. Soc.* **1951**, *106*, 241–307. [CrossRef]

51. Wheeler, J.; Park, R.G.; Rollinson, H.R.; Beach, A. The Lewisian Complex: insights into deep crustal evolution. *Geol. Soc. Lond., Spec. Publ.* **2010**, *335*, 51–79. [CrossRef]

52. Sheraton, J.W.; Skinner, A.C.; Tarney, J. The geochemistry of the Scourian gneisses of the Assynt district. In *The Early Precambrian Rocks of Scotland and Related Rocks of Greenland*; University of Keele: Keele, UK, 1973; pp. 13–30.

53. Park, R.G.; Tarney, J. The Lewisian complex: a typical Precambrian high-grade terrain? *Geol. Soc. London, Spec. Publ.* **1987**, *27*, 13–25. [CrossRef]

54. Kinny, P.; Friend, C.; Love, G. Proposal for a terrane-based nomenclature for the Lewisian Gneiss Complex of NW Scotland. *J. Geol. Soc. Lond.* **2005**, *162*, 175–186. [CrossRef]

55. Love, G.J.; Friend, C.R.L.; Kinny, P.D. Palaeoproterozoic terrane assembly in the Lewisian Gneiss Complex on the Scottish mainland, south of Gruinard Bay: SHRIMP U-Pb zircon evidence. *Precambrian Res.* **2010**, *183*, 89–111. [CrossRef]

56. Kinny, P.D.; Friend, C.R.L. U-Pb isotopic evidence for the accretion of different crustal blocks to form the Lewisian Complex of northwest Scotland. *Contrib. Mineral. Petrol.* **1997**, *129*, 326–340. [CrossRef]

57. Friend, C.R.L.; Kinny, P.D. A reappraisal of the Lewisian Gneiss Complex: geochronological evidence for its tectonic assembly from disparate terranes in the Proterozoic. *Contrib. Mineral. Petrol.* **2001**, *142*, 198–218. [CrossRef]

58. Love, G.J.; Kinny, P.D.; Friend, C.R.L. Timing of magmatism and metamorphism in the Gruinard Bay area of the Lewisian Gneiss Complex: Comparisons with the Assynt Terrane and implications for terrane accretion. *Contrib. Mineral. Petrol.* **2004**, *146*, 620–636. [CrossRef]

59. Park, R.G. The Lewisian terrane model: a review. *Scott. J. Geol.* **2005**, *41*, 105–118. [CrossRef]

60. Goodenough, K.M.; Park, R.G.; Krabbendam, M.; Myers, J.S.; Wheeler, J.; Loughlin, S.C.; Crowley, Q.G.; Friend, C.R.L.; Beach, A.; Kinny, P.D.; Graham, R.H. The Laxford Shear Zone: An end-Archaean terrane boundary? *Geol. Soc. Lond., Spec. Publ.* **2010**, *335*, 103–120. [CrossRef]

61. Goodenough, K.M.; Crowley, Q.G.; Krabbendam, M.; Parry, S.F. New U-Pb age constraints for the Laxford Shear Zone, NW Scotland: Evidence fortectono-magmatic processes associated with the formation of a Paleoproterozoic supercontinent. *Precambrian Res.* **2013**, *232*, 1–19. [CrossRef]

62. Crowley, Q.G.; Key, R.; Noble, S.R. High-precision U–Pb dating of complex zircon from the Lewisian Gneiss Complex of Scotland using an incremental CA-ID-TIMS approach. *Gondwana Res.* **2015**, *27*, 1381–1391. [CrossRef]

63. MacDonald, J.M.; Goodenough, K.M.; Wheeler, J.; Crowley, Q.; Harley, S.L.; Mariani, E.; Tatham, D. Temperature-time evolution of the Assynt Terrane of the Lewisian Gneiss Complex of Northwest Scotland from zircon U-Pb dating and Ti thermometry. *Precambrian Res.* **2015**, *260*, 55–75. [CrossRef]

64. Barooah, B.C.; Bowes, D.R. Multi-episodic modification of high-grade terrane near Scourie and its significance in elucidating the history of the Lewisian Complex. *Scott. J. Geol.* **2009**, *45*, 19–41. [CrossRef]

65. Corfu, F. U-Pb zircon systematics at Gruinard Bay, northwest Scotland: Implications for the early orogenic evolution of the Lewisian complex. *Contrib. Mineral. Petrol.* **1998**, *133*, 329–345. [CrossRef]

66. Feisel, Y.; White, R.W.; Palin, R.M.; Johnson, T.E. New constraints on granulite facies metamorphism and melt production in the Lewisian Complex, northwest Scotland. *J. Metamorph. Geol.* **2018**, *36*, 799–819. [CrossRef]

67. Andersen, T.; Whitehouse, M.J.; Burke, E.A.J. Fluid inclusions in Scourian granulites from the Lewisian complex of NW Scotland: Evidence for CO2-rich fluid in Late Archaean high-grade metamorphism. *Lithos* **1997**, *40*, 93–104. [CrossRef]

68. Park, R.G. The structural history of the Lewisian rocks of Gairloch, Wester Ross, Scotland. *Q. J. Geol. Soc.* **1964**, *120*, 397–426. [CrossRef]

69. Beach, A. The mineralogy of high temperature shear zones at Scourie, N.W. Scotland. *J. Petrol.* **1973**, *14*, 231–248. [CrossRef]

70. Attfield, P. The structural history of the Canisp Shear Zone. *Geol. Soc. Lond. Spec. Publ.* **1987**, *27*, 165–173. [CrossRef]

71. Corfu, F.; Heaman, L.M.; Rogers, G. Polymetamorphic evolution of the Lewisian complex, NW Scotland, as recorded by U-Pb isotopic compositions of zircon, titanite and rutile. *Contrib. Mineral. Petrol.* **1994**, *117*, 215–228. [CrossRef]

72. Davies, J.H.F.L.; Heaman, L.M. New U-Pb baddeleyite and zircon ages for the Scourie dyke swarm: A long-lived large igneous province with implications for the Paleoproterozoic evolution of NW Scotland. *Precambrian Res.* **2014**, *249*, 180–198. [CrossRef]

73. Heaman, L.M.; Tarney, J. U–Pb Baddeleyite ages for the Scourie Dyke Swarm, Scotland—Evidence for 2 distinct intrusion events. *Nature* **1989**, *340*, 705–708. [CrossRef]

74. Teall, J.J.H. The Metamorphosis of Dolerite into Hornblende-Schist. *Q. J. Geol. Soc.* **1885**, *41*. [CrossRef]

75. Beach, A.; Coward, M.P.; Graham, R.H. An interpretation of the structural evolution of the Laxford Front, north-west Scotland. *Scott. J. Geol.* **1974**, *9*, 297–308. [CrossRef]

76. Johnson, T.E.; Brown, M.; Goodenough, K.M.; Clark, C.; Kinny, P.D.; White, R.W. Subduction or sagduction? Ambiguity in constraining the origin of ultramafic-mafic bodies in the Archean crust of NW Scotland. *Precambrian Res.* **2016**, *283*, 89–105. [CrossRef]

77. O'Hara, M.J. Zoned ultrabasic and basic gneiss masses in the early lewisian metamorphic complex at scourie, Sutherland. *J. Petrol.* **1961**, *2*, 248–276. [CrossRef]

78. Bowes, D.R.; Park, R.G.; Wright, A.E. Layered intrusive rocks in the Lewisian of the North-West Highlands of Scotland. *Q. J. Geol. Soc.* **1964**, *120*, 153. [CrossRef]

79. Sills, J.D. Geochemical Studies of the Lewisian Complex of the Western Assynt Region, NW Scotland. Ph.D. Thesis, University of Leicester, Leicester, UK, January 1981.

80. Sills, J.D.; Savage, D.; Watson, J.V.; Windley, B.F. Layered ultramafic-gabbro bodies in the Lewisian of northwest Scotland: Geochemistry and petrogenesis. *Earth Planet. Sci. Lett.* **1982**, *58*, 345–360. [CrossRef]

81. Rollinson, H.; Gravestock, P. The trace element geochemistry of clinopyroxenes from pyroxenites in the Lewisian of NW Scotland: Insights into light rare earth element mobility during granulite facies metamorphism. *Contrib. Mineral. Petrol.* **2012**, *163*, 319–335. [CrossRef]

82. McDonald, I.; Viljoen, K.S. Platinum-group element geochemistry of mantle eclogites: a reconnaissance study of xenoliths from the Orapa kimberlite, Botswana. *Appl. Earth Sci.* **2006**, *115*, 81–93. [CrossRef]

83. Babechuk, M.G.; Kamber, B.S.; Greig, A.; Canil, D.; Kodolányi, J. The behaviour of tungsten during mantle melting revisited with implications for planetary differentiation time scales. *Geochim. Cosmochim. Acta* **2010**, *74*, 1448–1470. [CrossRef]

84. Govindaraju, K. Compilation of working values and samples description for 383 geostandards. *Geostand. Newsl.* **1994**, *18*, 1–158. [CrossRef]

85. Ottley, C.J.; Pearson, D.G.; Irvine, G.J. A routine method for the dissolution of geological samples for the analysis of REE and trace elements via ICP-MS. In *Plasma Source Mass Spectrometry: Applications and Emerging Technologies*; Holland, G., Tanner, S.D., Eds.; The Royal Society of Chemistry: Cambridge, UK, 2003; pp. 221–230.

86. Droop, G.T.R. A General Equation for Estimating Fe^{3+} Concentrations in Ferromagnesian Silicates and Oxides from Microprobe Analyses, Using Stoichiometric Criteria. *Mineral. Mag.* **1987**, *51*, 431–435. [CrossRef]

87. Hughes, H.S.R.; McDonald, I.; Faithfull, J.W.; Upton, B.G.J.; Downes, H. Trace-element abundances in the shallow lithospheric mantle of the North Atlantic Craton margin: Implications for melting and metasomatism beneath Northern Scotland. *Mineral. Mag.* **2015**, *79*, 877–907. [CrossRef]

88. McDonough, W.F.; Sun, S.S. The composition of the Earth. *Chem. Geol.* **1995**, *120*, 223–253. [CrossRef]

89. Sun, S.S.; McDonough, W.F. Chemical and isotopic systematics of oceanic basalts: implications for mantle composition and processes. *Geol. Soc. Lond. Spec. Publ.* **1989**, *42*, 313–345. [CrossRef]

90. Rollinson, H. Geochemical constraints on the composition of Archaean lower continental crust: Partial melting in the Lewisian granulites. *Earth Planet. Sci. Lett.* **2012**, *351–352*, 1–12. [CrossRef]

91. Williams-Jones, A.E.; Migdisov, A.A.; Samson, I.M. of the Rare Earth Elements—a Tale of "Ceria" and "Yttria". *Elements* **2012**, *8*, 355–360. [CrossRef]

92. Beach, A.; Tarney, J. Major and trace element patterns established during retrogressive metamorphism of granulite-facies gneisses, NW Scotland. *Precambrian Res.* **1978**, *7*, 325–348. [CrossRef]

93. Yaxley, G.M.; Crawford, A.J.; Green, D.H. Evidence for carbonatite metasomatism in spinel peridotite xenoliths from western Victoria, Australia. *Earth Planet. Sci. Lett.* **1991**, *107*, 305–317. [CrossRef]

94. Yaxley, G.M.; Green, D.H.; Kamenetsky, V. Carbonatite Metasomatism in the Southeastern Australian Lithosphere. *J. Petrol.* **1998**, *39*, 1917–1930. [CrossRef]

95. Babechuk, M.G.; Kamber, B.S. An estimate of 1.9 Ga mantle depletion using the high-field-strength elements and Nd-Pb isotopes of ocean floor basalts, Flin Flon Belt, Canada. *Precambrian Res.* **2011**, *189*, 114–139. [CrossRef]

96. Collerson, K.D.; Kamber, B.S. Evolution of the continents and the atmosphere inferred from Th-U-Nb systematics of the depleted mantle. *Science* **1999**, *283*, 1519–1522. [CrossRef] [PubMed]

97. Condie, K.C. Incompatible element ratios in oceanic basalts and komatiites: Tracking deep mantle sources and continental growth rates with time. *Geochem. Geophy. Geosyst.* **2003**, *4*, 1–28. [CrossRef]